© 2020. Published by The Company of Biologists Ltd | Journal of Cell Science (2020) 133, jcs232470. doi:10.1242/jcs.232470

RESEARCH ARTICLE

Senescent mesenchymal stem cells remodel extracellular matrix driving breast cancer cells to a more-invasive phenotype

Deepraj Ghosh[1], Carolina Mejia Pena[2], Nhat Quach[1], Botai Xuan[1], Amy H. Lee[3] and Michelle R. Dawson[1,2,3,*]

ABSTRACT

Mesenchymal stem cells (MSCs) are essential for the regenerative process; however, biological aging and environmental stress can induce senescence – an irreversible state of growth arrest – that not only affects the behavior of cells but also disrupts their ability to restore tissue integrity. While abnormal tissue properties, including increased extracellular matrix stiffness, are linked with the risk of developing breast cancer, the role and contribution of senescent MSCs to the disease progression to malignancy are not well understood. Here, we investigated senescence-associated biophysical changes in MSCs and how this influences cancer cell behavior in a 3D matrix interface model. Although senescent MSCs were far less motile than pre-senescent MSCs, they induced an invasive breast cancer phenotype, characterized by increased spheroid growth and cell invasion in collagen gels. Further analysis of collagen gels using second-harmonic generation showed increased collagen density when senescent MSCs were present, suggesting that senescent MSCs actively remodel the surrounding matrix. This study provides direct evidence of the pro-malignant effects of senescent MSCs in tumors.

KEY WORDS: Breast cancer, Tumor microenvironment, Cancer cell invasion, ECM remodeling, Mesenchymal stem cells, Senescence, Cell motility

INTRODUCTION

Mesenchymal stem cells (MSCs) are multipotent progenitor cells that reside in bone marrow and connective tissues and differentiate into multiple cell types required for normal tissue maintenance and repair. Homing of MSCs to tumors has been documented in multiple cancer types, including breast (Studeny et al., 2002), colon (O'Malley et al., 2016) and ovarian carcinomas (McLean et al., 2011), and gliomas (Ho et al., 2013). MSCs modulate the behavior of other cells by secreting signaling molecules, matrix proteins or enzymes to alter their function (Caplan and Dennis, 2006). These MSC-secreted factors can modulate tumor bystander effects after radiotherapy (De Araújo Farias et al., 2015), suppress the immune response to tumors (Uccelli et al., 2008) and drive the formation of more invasive cancer cell phenotypes (Karnoub et al., 2007; McAndrews et al., 2015b). MSCs also differentiate into carcinoma-associated fibroblasts (CAFs), which play a central role in tumor growth and matrix remodeling by increasing matrix deposition, crosslinking and bundling for increased tissue stiffness (Orimo et al., 2005; Kalluri and Zeisberg, 2006), activating mechanosensitive signaling pathways (Kümper and Marshall, 2011), and generating force and protease-mediated tracks that cancer cells can follow during metastasis (Carey et al., 2017). MSCs are highly resistant to apoptosis (Vallabhaneni et al., 2016) but undergo senescence in response to DNA damage, replicative stress or genotoxic stress from environmental toxins, therapeutic agents or ionizing radiation (Kasper et al., 2009; Wagner et al., 2009; Alessio et al., 2015). Growth is irreversibly arrested in senescent cells; however, they remain metabolically active and develop a senescence-associated secretory phenotype (SASP) (Acosta et al., 2013) that may contribute to tissue fibrosis and cancer progression (Acosta et al., 2013; Lunyak et al., 2017).

The detrimental effects of accumulating senescent cells on tissues have long been recognized (Campisi, 2013); this contributes to biological aging, tissue degeneration and cancer (Muñoz-Espín and Serrano, 2014). Pro-inflammatory molecules and degrading enzymes in the SASP contribute to cancer progression through recruitment and differentiation of other stromal cells (Rodier and Campisi, 2011), increased proliferation, motility and invasiveness of cancer cells (Mathon and Lloyd, 2001), and remodeling of the extracellular matrix (ECM) to promote cancer cell invasion and metastasis (Muñoz-Espín and Serrano, 2014). In previous studies, senescent stromal cells enhanced the growth and malignant transformation of mammary epithelial cells (Krtolica et al., 2001), promoted more rapid growth of malignant tumors (Liu and Hornsby, 2007), and caused tumor dormancy and treatment resistance when they were 'cannibalized' by breast cancer cells (BCCs) (Bartosh et al., 2016). Furthermore, non-motile BCCs treated with SASP factors (including IL-6, IL-8, and senescent fibroblast conditioned medium) undergo dramatic cytoskeletal reorganization as they transitioned to more aggressive migratory phenotypes (Aifuwa et al., 2015). SASP factors also stimulated the migration of cancer cells in 2D (Ortiz-Montero et al., 2017) and branching of tumor organoids in 3D collagen gels (Parrinello et al., 2005). Senescence is also associated with enhanced exosome secretion (Kadota et al., 2018); in fact, senescence-associated exosomes are potent SASP factors that transfer inflammatory cytokines, miRNAs and receptors important in breast cancer progression (Lehmann et al., 2008). The SASP has also been shown to alter ECM remodeling to drive pulmonary fibrosis (Cárdenes et al., 2018) and age-related muscle decline (Stearns-Reider et al., 2017). The effect of matrix stiffening on tumor progression is widely recognized (Paszek et al., 2005), and carcinoma-associated ECM is considered an integral feature of malignant breast cancers (Levental et al., 2009; Luo et al., 2015). The increased stiffness induces a malignant phenotype in epithelial cells (Paszek et al., 2005), promotes tumor progression (Levental et al., 2009), and is critical for the generation and maintenance of CAFs (Calvo et al., 2013). Multiple studies have investigated pro-inflammatory and immunomodulatory effects of senescent MSCs on tissues (Turinetto et al., 2016; Lunyak et al., 2017).

[1]Brown University, Department of Molecular Pharmacology, Physiology, and Biotechnology, Providence, RI 02912, USA. [2]Brown University, Department of Molecular Biology, Cell Biology and Biochemistry, Providence, RI 02912, USA. [3]Brown University, Center for Biomedical Engineering, Providence, PI 02912, USA.

*Author for correspondence (michelle_dawson@brown.edu)

M.R.D., 0000-0002-2122-4711

Received 27 March 2019; Accepted 19 December 2019

In this study, we investigated senescence-associated changes in the matrix remodeling induced by MSCs. Senescent MSCs were larger and less motile, with dense actin stress fibers and focal adhesions throughout. These changes severely limited their ability to polarize and migrate in both 2D and 3D environments. Molecular pathways that regulate cell biophysical properties and ECM remodeling were highly dysregulated, and key proteins involved in matrix stiffening were upregulated, including lysl oxidase (LOX), periostin (POSTN) and multiple collagen isoforms. Senescent MSCs also deposited and cross-linked ECM proteins, altering the architecture and mechanics of the surrounding collagen network. To study the heterotypic interaction of senescent MSCs with BCCs, we developed a 3D matrix interface model which allowed for quantitative analysis of single-cell migration from spheroids into the surrounding ECM. Although senescent MSCs were far less motile than pre-senescent MSCs, they continued to deposit and crosslink the collagen network to alter the behavior of BCCs. Matrix remodeling by senescent MSCs was associated with increased proliferation and motility of BCCs. Molecular inhibitors targeting senescence-induced matrix remodeling diminished this invasive BCC phenotype. These findings demonstrate the critical role senescence-induced matrix remodeling may play in age-related cancer progression.

RESULTS

Senescent MSCs are larger with altered cytoskeletal and focal adhesion organization

Early passage pre-senescent MSCs were treated with 15 Gy γ-irradiation (with a Mark I 68A ^{137}Cs irradiator) (Marthandan et al., 2016) to induce senescence. After 10 days, senescence was confirmed based on increased expression of senescence-associated β-galactosidase enzyme and reduced incorporation of bromodeoxyuridine (BrdU) (Fig. S1A,B). Additionally, we confirmed gene expression panel of previously described SASP markers including the cell cycle regulatory factors P16 (also known as CDKN2A) and APO1 (also known as FAS), and pro-inflammatory cytokines IL6, IL8 and IL1β in the senescent MSCs using quantitative real-time RT-PCT (qRT-PCR) (Fig. S1C). Enlarged size and irregular shape are key features of senescent cells; thus, we investigated how the cell and nuclear organization were altered in senescent versus pre-senescent MSCs (Fig. 1A,B). The morphological analysis showed a dramatic increase in both the cell (>4-fold) and nuclear area (>2-fold) (Fig. 1B). Immunostaining for actin and vinculin illustrated that senescent MSCs had a poorly organized actin structure with focal adhesions distributed throughout the cells, not localized to the tips of actin stress fibers, as seen in pre-senescent MSCs (n>15 cells) (Fig. 1A). Image analysis was used to quantify differences in adhesive polarity based on the location of vinculin-stained focal adhesions. For pre-senescent MSCs, focal adhesion size increased linearly with distance from the centroid, with the largest focal adhesions near the cell cortex (Fig. 1C). In contrast, focal adhesion size was independent of distance from the centroid, and larger focal adhesions were often found closer to the centroid in senescent MSCs (Fig. 1C). Furthermore, F-actin structure analysis confirmed that larger actin stress fibers appeared in senescent MSCs (∼10% increase) (Fig. 1C). These changes in cytoskeletal architecture may contribute to altered mechanical properties in the cell, which regulate dynamic cell processes such as migration.

Reduced heterogeneity in cytoskeletal and nuclear mechanics

Intracellular particle tracking was used to determine the local mechanical properties of the cytoplasm from the thermal displacements of particles embedded in the cell. This technique uses video tracking technology to probe the motion of fluorescent nanoparticles over short time periods (less than 1 min). The time-dependent particle mean squared displacements (MSDs) can easily be related to local mechanical properties of the surrounding fluid or ensemble-averaged to determine bulk mechanical properties (Tseng et al., 2002; Dawson et al., 2014). In a purely viscous fluid, particles move diffusively with MSDs that vary linearly with time; however, when particles are embedded in a viscoelastic fluid, like the cell cytoplasm, particle motion is much more restricted due to entrapment in the surrounding structure, and MSD slopes become less than 1. Since these mechanical properties are determined from the transport rates of hundreds of individual particles, intracellular particle tracking can be used to probe for intracellular heterogeneity based on the variation in particle transport rates. The resulting distribution in MSDs offers insight into the degree of mechanical heterogeneity and can be connected to the spatial distribution of actin crosslinking and subcellular microstructure (Kole et al., 2005). Intracellular particle tracking was used to quantify differences in cytoskeletal mechanics (n>15 cells/group, 10–20 particles/cells, n>200 particles/group) for pre-senescent and senescent MSCs (Fig. 1D) based on our previously established protocols (McGrail et al., 2012; Ghosh et al., 2014). The amplitude and logarithmic slope ($\alpha \approx 1$) of MSDs for both population of MSCs indicated that the particle motions are less restricted in the cytoplasm, suggesting that viscoelastic behavior of the cytoplasmic network is dominated by viscous properties that are similar to our previously reported values in MSCs and metastatic cancer cells (McGrail et al., 2013; Dawson et al., 2014). The ensemble averaged MSDs (indicated by dark lines) were comparable between pre-senescent and senescent MSCs, indicating similarity in their bulk mechanical properties; however, the reduced heterogeneity in individual particle MSDs for senescent MSCs suggests their mechanical properties are more homogeneous than pre-senescent MSCs (Fig. 1D). This reduced heterogeneity in cytoskeletal mechanics is further illustrated by a reduced coefficient of variation (CV) in MSD values at t=1 and 10 s (Fig. 1D).

Particle tracking of Hoechst 33342-labeled chromatin granules was used to probe for differences in nuclear mechanics (Fig. 1E) (Xuan et al., 2018). At short time scales ($\ll$1 s), the MSDs remained constant, whereas, at longer time scales, the MSDs varied linearly with time for both cell types. This inflection point represents a transition from elastic to viscous fluid properties that is referred to as the relaxation point. Again, we see little difference in the ensemble averaged MSDs for both groups, with less variation in individual particle MSDs for senescent MSCs (Fig. 1E). This reduced heterogeneity in particle transport rates was significant at long time scales ($\gg$1 s) after the relaxation had occurred. These data indicate that the bulk nuclear mechanical properties of senescent MSCs are similar, although more homogeneous than in pre-senescent MSCs. Interestingly, the relaxation point was significantly reduced in senescent MSCs (Fig. S1D), signifying a faster transition to a softer nucleus, suggesting some fundamental difference in nuclear deformation.

Senescent MSCs lose their migratory capacity

Next, we investigated how alterations in cell structure affect dynamic cell processes such as migration. We tracked 2D migration of over 500 cells per condition and found senescent MSCs to be significantly less motile than pre-senescent MSCs (Fig. 2A). In addition to reduced motility, senescent MSCs also moved less directionally. Migration of MSCs in 3D collagen gels

Journal of Cell Science (2020) 133, jcs232470. doi:10.1242/jcs.232470

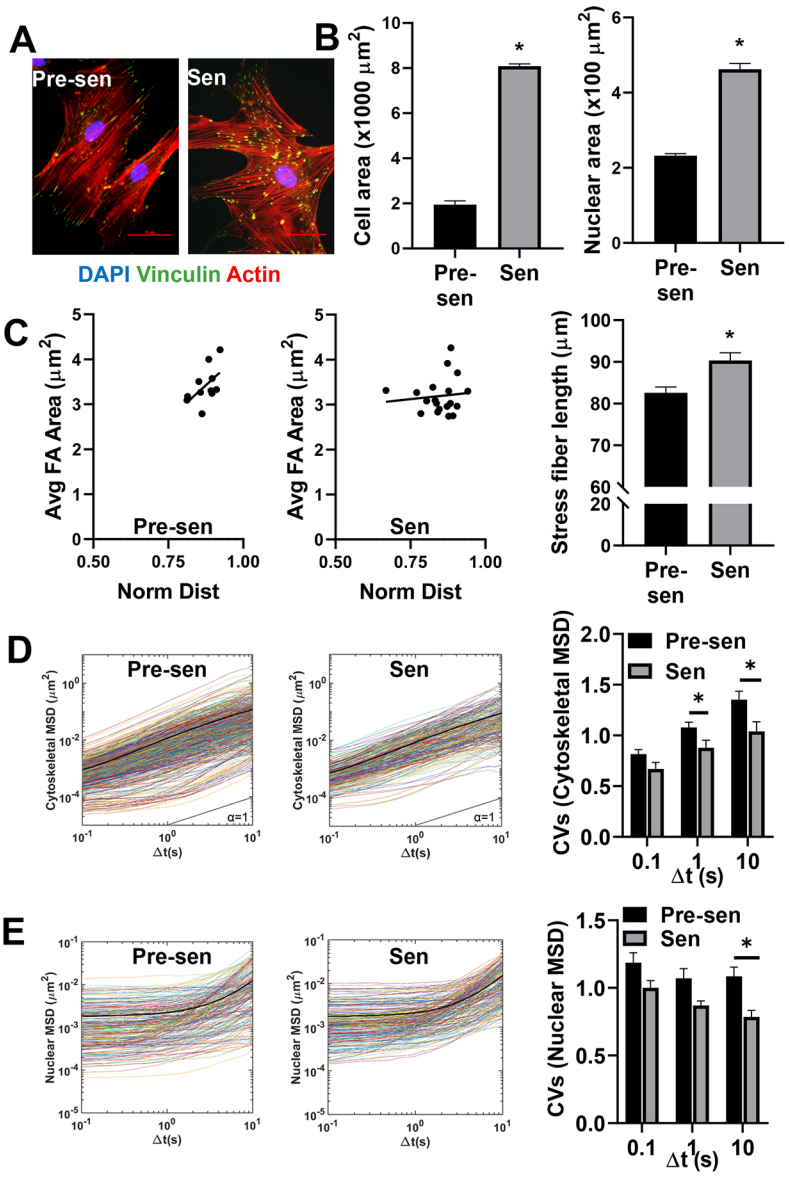

Fig. 1. Senescent MSCs displayed altered, cytoskeletal and nuclear organization and mechanics. Human MSCs were treated with 15 Gy γ-irradiation to induce senescence. (A) Immunostaining for vinculin (green), actin (red), and DAPI (blue) was used to visualize the actin organization and focal adhesion (FA) distribution of pre-senescent (Pre-sen) and senescent (Sen) MSCs. Scale bars: 50 µm. (B) Quantification of physical cell parameters revealed senescence induced a significant increase in the cell and nuclear area. (C) Scatter plot of average FA area (Avg FA Area) against the normalized distance (Norm Dist) of FAs from the centroid of the cell demonstrated the altered distribution between pre-senescent and senescent cells. FA size increased more sharply with distance from the centroid in pre-senescent MSCs compared to in senescent MSCs. Average stress fiber length increased by ∼10% in senescent cells compared to the control. (D) Cytoskeletal mechanics was assessed by tracking the motion of 200-nm probe particles embedded in the cytosol (n>15 cells/condition, n=10–20 particles/cells, n>200 particles/condition). Time-dependent ensemble average MSDs increased linearly with time-scale for both pre-senescent and senescent MSCs; however, the MSD distributions were narrower for senescent MSCs. Colored lines represent individual traces from each particle MSD, whereas the black line represents the ensemble average MSD of all particles. Coefficient of variations (CVs) were calculated for cytoskeletal MSDs at t=0.1, t=1 and t=10 s. Pre-senescent MSCs displayed significantly higher CVs compared to senescent cells at t=1 and t=10 s. (E) Nuclear mechanics was assessed by tracking Hoechst 33342-labeled chromatin in the nuclei. At short time-scales (≪ 1 s) the MSDs were independent of time, resembling particle motion in more elastic material; however, at later time scales (≫ 1 s) nuclei transitioned to more viscous behavior, as indicated by an increasing MSD slope. Colored lines represent traces from each tracked condensed chromatin spot, whereas the black line represents the ensemble average of all tracks. CVs were calculated for nuclear (Nuc) MSDs at t=0.1, t=1 and t=10 s. Pre-senescent MSCs displayed significantly higher CVs compared to senescent cells at t=10 s. Results are mean±s.e.m.; *P<0.05 (Student's t-test).

followed a similar trend; the mean velocity of pre-senescent MSCs was more than 2-fold higher than that of senescent MSCs (Fig. 2B). Mesenchymal migration in 3D collagen gels is characterized by the formation of integrin-based adhesions and dendritic protrusions at the leading edge of a cell, followed by nuclear elongation in the direction of migration, and branching of protrusions to support the migration of polarized cells along collagen fibers (Wu et al., 2018). Both cell types formed integrin-based adhesions and dendritic protrusions; however, only pre-senescent MSCs were able to polarize these protrusions for directional cell migration (Fig. 2B). We quantified this observation based on the ratio of leading edge to trailing edge protrusions. For senescent MSCs, this ratio was ∼1, further demonstrating the loss in cell polarity with senescence. This ratio was increased up to 50% for pre-senescent MSCs, in part to the large number of migrating cells (Fig. 2B). In addition to the polarized binding and the formation of adhesive protrusions at the leading edge of the cell, the ability for cells to migrate in 3D environments is largely regulated by nuclear size, shape and rigidity (Wolf et al., 2003). Senescent MSCs had larger but slightly more elongated nuclei than pre-senescent MSCs. Thus, the nuclear shape factor of senescent MSCs was reduced (Fig. 2C). However, pre-senescent MSCs more readily altered their nuclear shape (ΔNSF), allowing them to squeeze through smaller pores. This is further illustrated by their lower feret diameters, since the minimum feret diameter represents the smallest pore size an elongated nucleus can squeeze through (Fig. 2C). Overall, the loss of migration of senescent MSCs correlated with their larger and less deformable nuclei, and inability to adjust cell polarity sufficiently to move in confined collagen-rich environments.

Senescence induces significant variations in protein expression

To understand the senescence-induced molecular changes in MSCs, a mass spectrometry-based proteomics analysis was carried out. A total of 1134 unique proteins were significantly regulated in senescent MSCs compared to pre-senescent MSCs. Of these differentially altered proteins, 116 were related to nuclear or cytoskeletal structure. A small number of the significantly downregulated (green) and upregulated (red) proteins are listed in Fig. 3A and Fig. S2. Actin-binding proteins that increase the stability of actin cytoskeleton were

Journal of Cell Science (2020) 133, jcs232470. doi:10.1242/jcs.232470

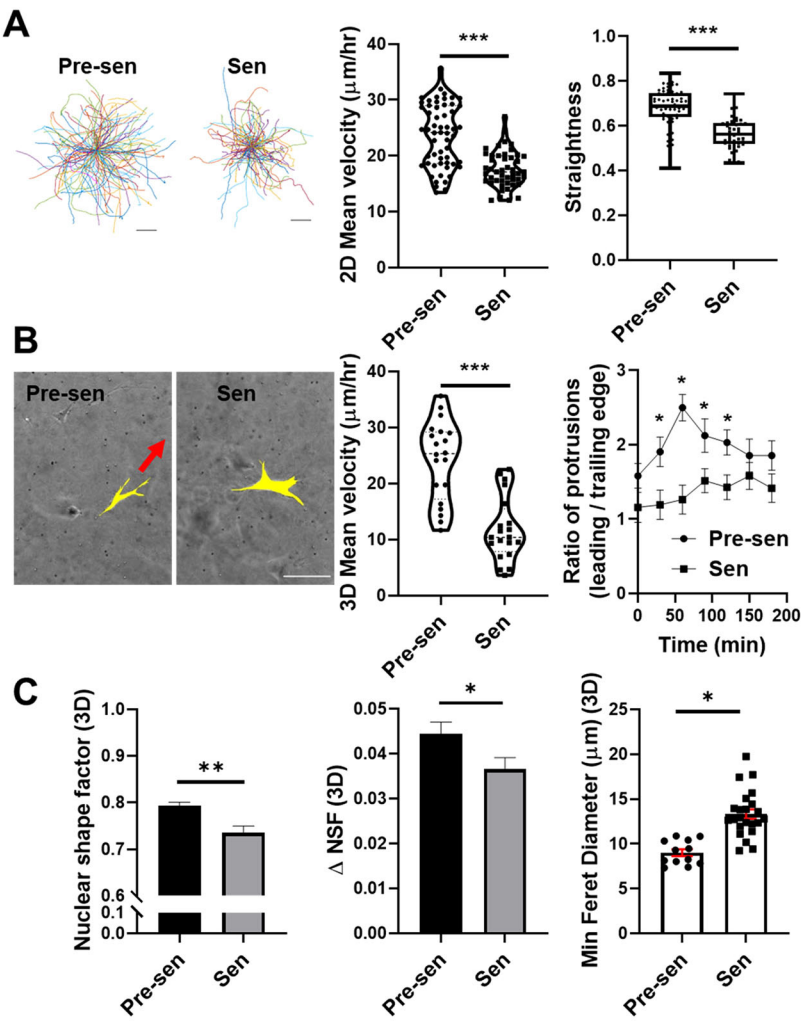

Fig. 2. Senescence reduced MSC migration significantly in 2D and 3D. (A) Representative traces of single-cell motions for pre-senescent (Pre-sen) and senescent (Sen) MSCs and dot plots representing single-cell mean velocities, assessed by tracing the motion of Hoechst 33342-stained nuclei over 12-h time period at 10 min intervals. Straightness of cell migration was calculated using total path length over net displacement to assess persistent motion and is shown as a box-and-whisker plot, where the box represents the 25–75th percentiles, and the median is indicated. The whiskers show the minimum and maximum value of the data points. (B) MSCs were embedded in collagen and imaged at 15-min intervals over a 12-h time period. Pre-senescent MSCs formed leading edge protrusions in the direction of migration, whereas senescent MSCs formed protrusions in multiple directions but were unable to move forward. Scale bar: 100 µm. Based on nuclear *xy* coordinates, we tracked hundreds of individual cells for each condition; the mean velocity of senescent MSCs was reduced (P<0.001). For both cell types, leading edge and trailing edge protrusions were counted; we report the mean±s.e.m. ratio of leading to trailing edge protrusions, which characterizes the likelihood of cells being able to move forward. (C) Nuclear shape factor (NSF), change in NSF (ΔNSF), and minimum feret diameter were quantified for MSCs in 3D collagen gels. Senescent MSC nuclei were slightly more elongated but less deformable resulting in higher feret diameters that limited their migration in porous collagen networks. Results are mean±s.e.m. *P<0.05, **P<0.01, ***P<0.001 (Student's *t*-test).

upregulated with senescence; these included cortactin (CTTN), α-actinin 2 (ACTN2) and adducins (ADD1 and ADD3). We previously reported similar changes in actin-binding protein expression in TGF-β1-treated MSCs, which resulted in homogeneous stiffening of the cytosol and development of a CAF-like phenotype (Ghosh et al., 2014). In addition, proteins that control microtubule dynamics, including the microtubule-associated proteins MAPRE1 (EB1), MAP1B and MAP4, were collectively downregulated in senescent MSCs. Additionally, proteins that control the dynamics of nuclear structure, including proteins that are part of LINC complexes (SUN2), the nuclear lamina (LMNB1 and LBR), the nuclear matrix (MATR3), and nuclear pore complexes (IPO7 and IPO11) were downregulated in senescent MSCs. Loss of LMNB1 has been associated with cellular senescence and biological aging (Dahl et al., 2006). While the expression of integrins (ITGA2, ITGB5 and ITGB1) and focal adhesion proteins (VCL) was increased, cell–cell adhesion molecules (ALCAM and MCAM) were downregulated (Fig. 3B). Furthermore, ERM proteins (EZR and MSN) that link the cytoskeleton to the plasma membrane and transfer signals to regulate polarization in adhesion dependent processes and membrane dynamics were downregulated. Altogether, these results further support the idea that senescence results in a less-dynamic cytoskeletal structure that is not capable of cell polarization to drive cell motility.

Interestingly, a significant number of proteins related to ECM synthesis and turnover were differentially expressed in senescent versus pre-senescent MSCs (Fig. 3B). These ECM proteins included multiple collagen isoforms (COL14, COL1 and COL6) and laminins (LAMC1 and LAMB1) found in the basement membrane. Fibril-associated collagens, such as COL14, are scaffolding collagens that contribute to the formation of dense ECM. COL6 is a non-fibrillar collagen important in matrix assembly and fibroblast motility in the skin (Theocharidis et al., 2016). Additionally, upregulation of matrix proteinases (MMP2), matrix proteinase inhibitors (TIMP1 and TIMP3), crosslinkers (TGM2 and LOX), and matricellular proteins (POSTN, THBS1 and VTN) suggest that senescent MSCs actively remodel the local microenvironment.

Senescent MSCs remodel the surrounding collagen matrix

Multiphoton microscopy was used to image collagen fibers surrounding carboxyfluorescein succinimidyl ester (CFSE)-labeled MSCs (Fig. 4A). Image analysis of 3D cell volume revealed that senescent MSCs were over 3-fold larger than pre-senescent MSCs (Fig. 4B). Both pre-senescent and senescent MSCs remodeled the local ECM, which caused differences in the local collagen architecture. To quantify the architecture of collagen surrounding cells, second-harmonic generation (SHG) images were analyzed using CurveAlign to calculate fiber properties including density and alignment. The coefficient of alignment, which varies between 0, for isotropic material, and 1, for perfectly aligned matrix, was higher for senescent MSCs compared to pre-senescent MSCs

Journal of Cell Science (2020) 133, jcs232470. doi:10.1242/jcs.232470

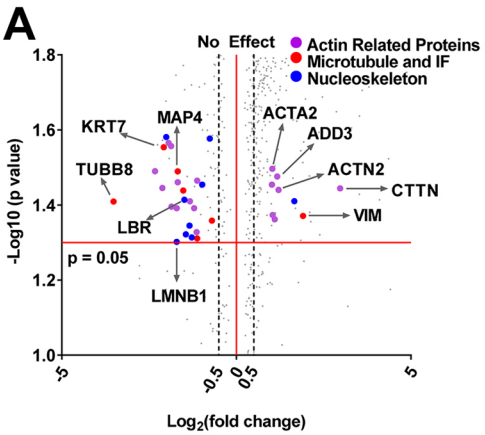

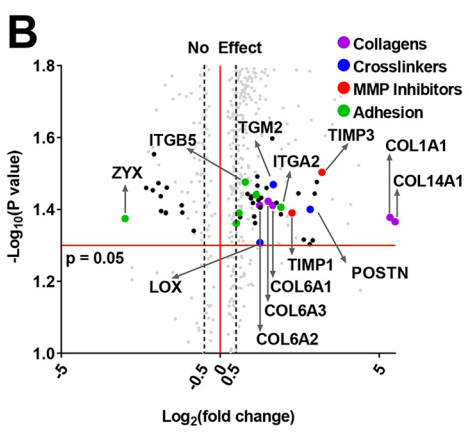

Actin		Microtubule and IFs	
Protein	log2(FC)	Protein	log2(FC)
CTTN	2.97	VIM	1.91
ACTN2	1.21	KRT19	-0.70
ADD3	1.17	MAPRE1	-1.12
ADD1	1.10	MAP1B	-1.52
CAPN2	1.04	MAP4	-1.68
ACTA2	1.03	KRT7	-2.08
MYO6	1.02	TUBB8	-3.52
ACTL6A	-1.12	IQGAP3	-6.16
TPM3	-1.14	Nucleoskeleton	
EZR	-1.21	PML	1.66
CNN3	-1.33	MATR3	-0.76
TPM2	-1.68	SUN2	-0.98
MSN	-1.71	TPR	-1.28
DIAPH1	-1.86	IPO11	-1.34
TAGLN2	-1.87	IPO7	-1.45
TAGLN	-1.94	LBR	-1.49
FLNC	-2.12	LMNB1	-1.71
CNN2	-2.33	KPNA7	-2.01

Collagens		Other ECM	
Protein	log2(FC)	Protein	log2(FC)
COL12A1	1.13	THBS1	0.63
COL6A2	1.24	FN1	0.86
COL4A2	1.46	TGFBI	1.07
COL6A3	1.51	BGN	1.15
COL5A2	1.64	SPARC	1.17
COL6A1	1.65	LAMC1	1.26
COL1A2	2.46	FBN1	1.29
COL4A1	2.82	LAMB1	2.63
COL1A1	5.34	POSTN	2.83
COL14A1	5.50	VTN	3.04
Matrix Modifying Enzymes			
TIMP1	2.26	LOX	1.25
MMP2	2.91	TGM2	1.67
TIMP3	3.20	P4HA1	1.77

Adhesion Molecules			
ZYX	-2.99	ITGBL1	0.79
ITGB1	0.51	ITGB5	1.13
VCL	0.59	ITGA2	1.91

Fig. 3. Mass spectrometric analysis of differentially regulated peptides in senescent versus pre-senescent MSCs. Comprehensive proteomic analysis was performed to find significantly (q value <0.05) changed peptides between the senescent and pre-senescent MSCs (n=4). The overall list of pathway specific genes was examined using gene ontology (GO) cellular component analysis. Differentially altered proteins are highlighted in gray in volcano plots, and critical genes are color-coded based on function. Log2 fold changes (FC) are also tabulated for key dysregulated genes. (A) Proteomic analysis was used to identify Log2 fold changes in the expression of cytoskeleton and nucleoskeleton related proteins for senescent versus pre-senescent MSCs, including actin-related proteins (magenta), microtubules and intermediate filaments (IFs) (red), and nucleoskeleton (blue). (B) Analysis of ECM related proteins was used to identify Log2 fold changes in expression of collagens, and other ECM proteins and crosslinkers for senescent MSCs compared to pre-senescent MSCs. Critical genes for ECM synthesis and turnover are highlighted in the volcano plot, including collagen isoforms (red), crosslinking proteins (blue), and MMP inhibitors (green). It is notable that POSTN, COL1A1, COL14A1 and TIMP3 are among the most highly upregulated proteins.

(Fig. 4B), indicating that collagen was aligned along cell surface. Additionally, the collagen density around senescent MSCs was increased, as indicated by the higher box density. Overall, senescent MSCs displayed an increased volume with a larger surface area for cell–ECM interactions, and significantly remodeled the surrounding matrix.

Both pre-senescent and senescent MSCs uniquely contribute to BCC invasion

To study the heterotypic interaction of MSCs with BCCs, we developed a 3D matrix interface model that allowed for quantitative analysis of single-cell migration from spheroids into surrounding ECM. Since MDA-MB-231 cells only form dense spheroids in the presence of stromal cells (Bartosh et al., 2016), an equal number of GFP-positive MDA-MB-231 cells were cultured with MSCs in suspension to form aggregates. To mimic the presence of both pre-senescent and senescent MSCs in the tumor, we created an additional mixed group with an equal number of pre-senescent and senescent MSCs. Inclusion of senescent MSCs in these cultures resulted in larger sized spherical aggregates (spheroids) (Fig. S3A, B). After 72 h, the aggregates were embedded in polymerized collagen to monitor the spreading and invasion of BCCs and MSCs from spheroids over a 16-h period (Fig. 5; Fig. S3). Senescent MSCs alone or in the mixed group induced an invasive BCC phenotype, characterized by an increase in spheroid size with time and increased number of protrusions after 16 h (Fig. 5B; Fig. S4A). Next, we quantified both the number of MSCs and BCCs escaping from spheroids (Fig. 5C,D). An interesting aspect to emerge from this study was the propensity of pre-senescent MSCs to invade the collagen gels (highlighted with the yellow cells in Fig. 5C). While pre-senescent MSCs invaded the matrix more rapidly with higher numbers, senescent MSCs promoted BCC invasion into collagen (highlighted with red cells in Fig. 5C). Presence of both attributes in the mixed population resulted in the highest level of both MSC and BCC invasion (Fig. 5, Fig. S3D).

The matrix-remodeling abilities of MSCs are crucial for BCC invasion

To further understand the organization of the cells in the spheroid and their interaction with the surrounding collagen matrix, multiphoton microscopy was used to image NucRed-labeled cells (both MSCs and BCCs), by means of fluorescence (shown in red), and collagen fibers, by means of SHG (shown in cyan) (Fig. 6A). The overlays of the average intensity projections highlight differences in cell density and packing between pre-senescent and senescent MSC-containing spheroids (Fig. 6A; Fig. S4C). Mobilization of the pre-senescent MSCs into the surrounding collagen correlated with spheroid cores

Journal of Cell Science (2020) 133, jcs232470. doi:10.1242/jcs.232470

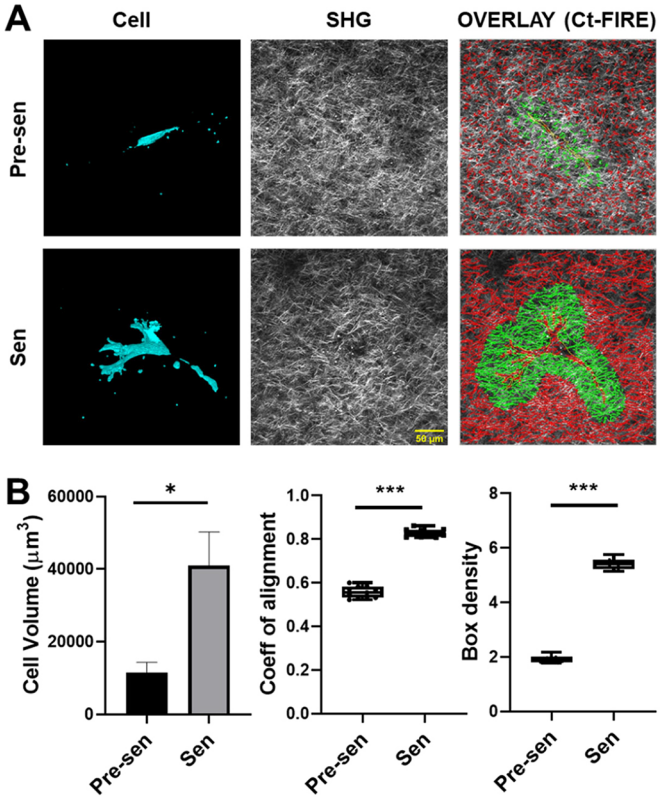

Fig. 4. MSC volume and matrix remodeling in 3D collagen gels. Pre-senescent (Pre-sen) and senescent (Sen) MSCs were embedded in collagen gels and incubated for 72 h. Then, the collagen gels were fixed and imaged using multiphoton microscopy for collagen fibers (gray, imaged through SHG) and MSCs (cyan, CFSE fluorescence). (A) A 3D reconstruction of MSCs along with corresponding processed SHG images showing the collagen density heatmap around cells, which was used to quantify physical parameters of the cells, and the surrounding ECM. Scale bar: 50 µm. (B) MSC volumes were calculated using the ImageJ voxel counter plugin, and ECM properties surrounding the cells were determined using CT-FIRE. Initially, cell boundaries were traced manually and saved as a mask. Subsequently, a uniform distance of 50 µm around the cell outline was used to determine the local fiber properties surrounding the cells including, coefficient of alignment and density (ROI highlighted in green in A). The volume of senescent MSCs was significantly larger. Additionally, both fiber alignment and density of the ECM surrounding senescent MSCs were significantly increased. Results are mean±s.e.m.; **P*<0.05, ****P*<0.001 (Student's *t*-test).

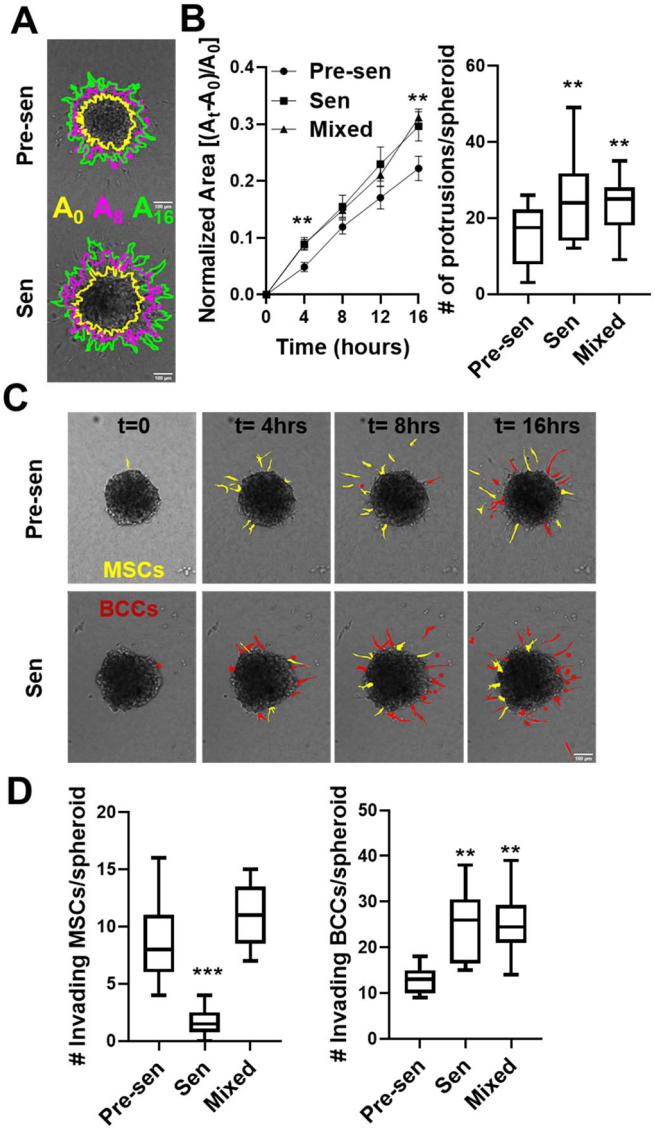

Fig. 5. Senescent MSCs promoted BCC invasion in a 3D matrix interface model. (A) Time-lapse imaging was used to monitor cell migration from spheroids using the matrix interface model. Spheroids formed from equal numbers of GFP-labeled BCCs and unlabeled MSCs [pre-senescent (Pre-sen), senescent (Sen) and mixed] were monitored over a 16 h period at 30-min intervals. Images of spheroid migration over time with regions highlighted in yellow, magenta and green depict the area at times, *t*=0, 8 and 16 h, respectively (A_0, A_8 and A_{16}). Scale bar: 100 µm. (B) Spheroid area over time was quantified. We report the mean±s.e.m. change in spheroid area normalized to initial area. The number of protrusions was calculated using temporal analysis of spheroid imaging (TASI) to assess the invasiveness of spheroids, and is shown as a box-and-whisker plot, where the box represents the 25–75th percentiles, and the median is indicated. The whiskers show the minimum and maximum value of the data points. (C) Time-lapse images of individual cell invasion are highlighted for invading MSCs in yellow and cancer cells in red. (D) We quantified the number of MSCs and BCCs that detached from spheroid surface and were individually invading the surrounding ECM. Senescent MSCs promoted collective spheroid invasion with increased normalized invaded area and increased number of protrusions as well as individual BCC invasion in collagen. Data are shown as box-and-whisker plots, where the box represents the 25–75th percentiles, and the median is indicated. The whiskers show the minimum and maximum value of the data points. ***P*<0.01, ****P*<0.001 (Student's *t*-tests).

becoming more hollow, whereas spheroids cultured with senescent MSCs remained relatively solid (Fig. 6A; Fig. S5). To quantify the architecture of surrounding collagen gels, SHG images were analyzed using CurveAlign to calculate fiber properties, including alignment and width. The coefficient of alignment, which varies between 0, for isotropic material, and 1, for perfectly aligned matrix, was higher in spheroids with pre-senescent and mixed MSC populations compared to that in senescent MSCs (Fig. 6B; Fig. S4). Average collagen fiber width was higher in senescent MSCs, suggesting more matrix bundling and/or crosslinking (Fig. 6C). Previous studies have found more collagen crosslinking with aging (Frantz et al., 2010; Phillip et al., 2015). Pre-senescent MSCs that readily migrated into the collagen may lead the way causing fiber alignment, whereas non-motile senescent MSCs can promote crosslinking of collagen surrounding the spheroid promoting stiffer local regions.

Finally, we probed whether the disruption of the MSC-mediated matrix remodeling could diminish the invasive behavior of BCCs in 3D. MMP activity was blocked by use of the inhibitor GM6001, and LOX was blocked with BAPN. Additionally, anti-POSTN antibody (POSTN-Ab) was used to determine whether the increased expression of this matricellular protein was a contributing factor

Journal of Cell Science (2020) 133, jcs232470. doi:10.1242/jcs.232470

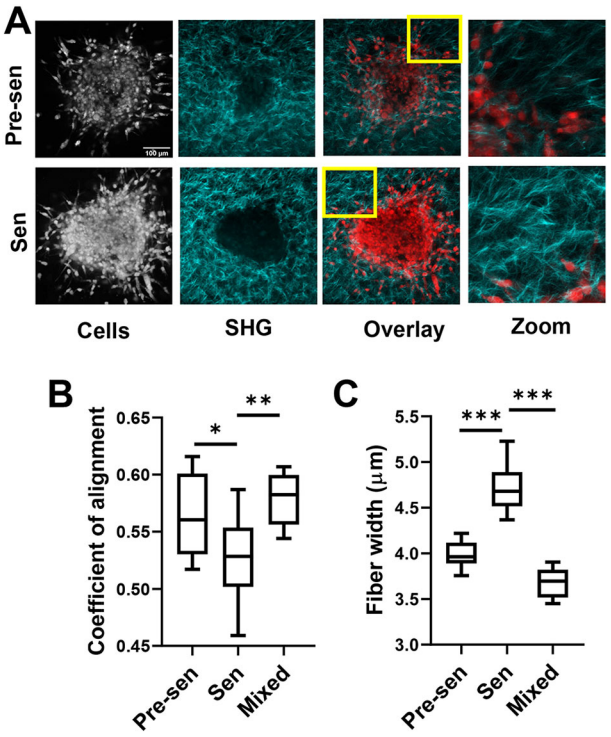

Fig. 6. Senescent MSCs rapidly remodeled the extracellular matrix. (A) Spheroids formed from BCCs and MSCs [pre-senescent (Pre-sen), senescent (Sen)] embedded in collagen gels were imaged by multiphoton microscopy using SHG to identify collagen (shown in cyan) and for NucRed fluorescence to identify cells. (B,C) SHG images were analyzed using CurveAlign to quantify collagen fiber properties and orientation. Coefficient of alignment measuring degree of collagen alignment surrounding spheroids was enhanced with pre-senescent cells (B), whereas collagen fiber width was increased for spheroids containing senescent cells only (C). Data are shown as box-and-whisker plots, where the box represents the 25–75th percentiles, and the median is indicated. The whiskers show the minimum and maximum value of the data points. *P<0.05, **P<0.01, ***P<0.001 (Student's t-tests).

to the more invasive BCC phenotype. After 16 h, GM6001, BAPN and POSTN-Ab abrogated cell invasion to different degrees (Fig. 7A–C). GM6001 was most efficient and completely able to block spheroid growth and individual BCC invasion for both pre-senescent and senescent MSC containing spheroids. Blocking LOX and POSTN did not affect the spheroids with pre-senescent MSCs; however, these blocking strategies resulted in decreased invaded area for spheroids with post-senescent MSCs. BAPN and POSTN-Ab were also able to partially block the individual cell invasion (P=0.052 for BAPN, P=0.083 for POSTN Ab).

DISCUSSION

Cellular senescence is a critical mechanism of limiting abnormal growth and cancer development; however, senescent cells accumulating in tumors can profoundly alter the biophysical properties of the tissue to force cancer progression toward malignancy. MSCs are present throughout vascularized tissues and survive for many years *in vivo* (Fehrer and Lepperdinger, 2005); this increases their risk for developing DNA damage from ionizing radiation, environmental toxins and chemotherapy, which can trigger senescence. Previous studies have shown that bone marrow-derived MSCs transition to a CAF phenotype after exposure to MDA-MB-231 BCCs (Mishra et al., 2008; Shangguan et al., 2012) and promote breast tumor growth (Karnoub et al., 2007; Lacerda et al., 2015). However, limited data is available to demonstrate the impact of senescence on MSC function in the tumor.

MSC senescence results in increased expression of ECM proteins and matrix-modifying enzymes, which can alter the composition and architecture of tissue environments to promote cancer progression. At low cell densities, this effect would only alter local regions of the collagen matrix; however, as senescent cells accumulate with age or genotoxic stress, this local matrix-remodeling effect may lead to abnormal collagen architectures and bulk matrix-stiffening effects. Changes in cell biophysical properties are essential in the development of this matrix remodeling phenotype. This is because cells sense and respond to forces from the ECM through mechanosensitive molecules in the cytoskeleton (Wang et al., 2009). The cytoskeletal proteins important in this process were highly dysregulated in senescent MSCs. Actin stress fibers formed by bundling and crosslinking of actin filaments (CTTN, ACTN and ADDs) were dramatically increased and microtubule-binding proteins (EB1 and MAPs), which regulate the dynamic structure of microtubules, were downregulated (Fig. 1; Fig. S2). These results correlated with a significantly reduced heterogeneity in intracellular mechanics in senescent MSCs, suggesting that the microstructure of this polymeric network is more homogeneous after senescence (Fig. 1D). Rapid remodeling of the cytoskeletal structure to maintain contractile cell phenotype is an energy-intensive process (Phillip et al., 2015). Thus, static mechanical properties in senescent cells may contribute to progressive metabolic changes and cells can utilize significant energy to maintain high production of SASP factors. These cytoskeletal changes may contribute to the larger and more stable size of senescent MSCs, and may also explain how non-proliferating cells are able to remain viable in the tissues for long periods of time. On the other hand, a less dynamic cytoskeletal network may limit the ability of the cell to respond to external stimuli, since differences in cell tension are important in transferring signals from the external environment to the nuclear lamina. Nuclear mechanics is mainly controlled by the structure of the nuclear lamina, along with underlying chromatin organization (Phillip et al., 2015; Stephens et al., 2017). Our proteomics analysis revealed HDAC and other histone cluster proteins were collectively downregulated in senescent MSCs (Fig. S2); the reduced expression of histone-modifying proteins in senescent MSCs may correlate with their faster transition from elastic to viscous nuclear mechanics (Stephens et al., 2017). Nuclear lamina proteins LMNB1 and LBR were significantly downregulated in senescent MSCs. The reduced expression of LMNB1 and LBR has been associated with loss of peripheral compact heterochromatin and wide-scale changes in DNA condensation that can correlate with the reduced heterogeneity in nuclear mechanics of senescent MSCs (Swanson et al., 2015; Criscione et al., 2016). Ferrera et al. reported reduced heterogeneity in nuclear stiffness in quiescent human skin fibroblasts compared to proliferating cells (Ferrera et al., 2014). While B-type lamins contribute to elastic resistance of the cells, lamin A (LMNA) has been associated with deformation-resistant viscous stiffness (Gruenbaum and Foisner, 2015; Lele et al., 2018). Increased LMNA expression correlated with a less-deformable nucleus (Harada et al., 2014). In our senescent MSCs, a combination of LMNB1 downregulation and LMNA upregulation (Fig. S2D) correlated with elongated but less-deformable nuclei.

Higher ratios of lamin A to lamin B have been shown to reduce nuclear deformability to inhibit cancer cell migration through pores (Swift et al., 2013; Harada et al., 2014). These overall changes in cytoskeletal and nuclear organization and mechanics can profoundly alter cell migration. Polarization of cytoskeletal and perinuclear actin results in anisotropy in actin structure and

Journal of Cell Science (2020) 133, jcs232470. doi:10.1242/jcs.232470

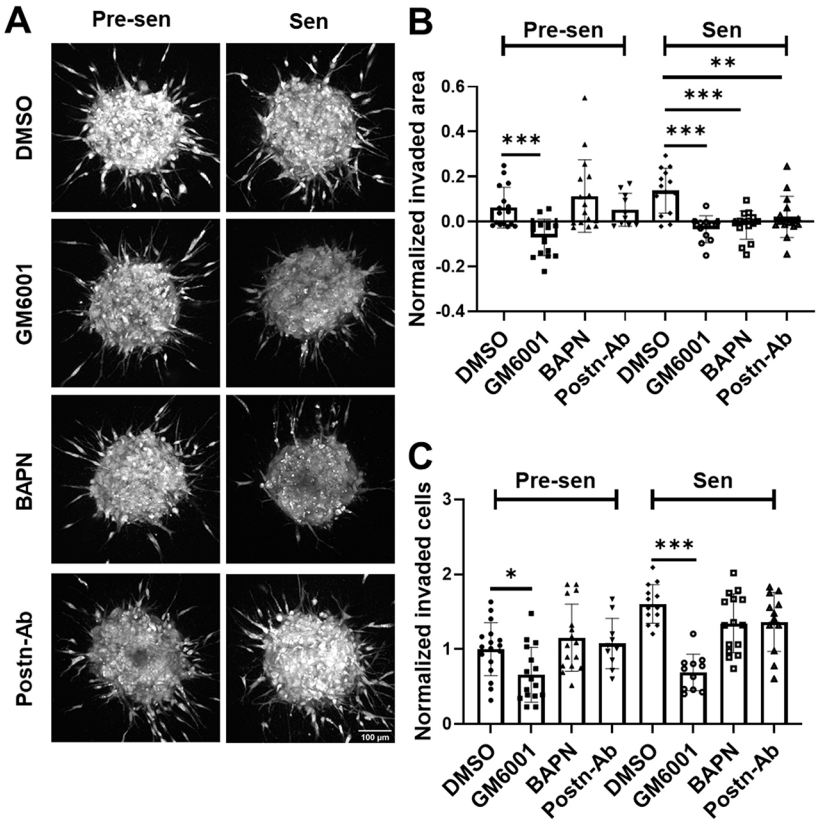

Fig. 7. Targeting senescence-associated ECM modifications to reverse invasive BCC phenotype. (A) Time-lapse imaging was used to monitor invasion over 16 h from spheroids formed through co-culture of MDA-MB-231 and pre-senescent (Pre-sen), senescent (Sen) MSCs. Spheroids were individually treated with small-molecule inhibitors for MMPs (GM6001), and LOX (BAPN), and neutralizing antibody for POSTN (Postn-Ab). Scale bar: 100 µm. We quantified (B) the normalized change in invaded area relative to initial area, and (C) number of invading cells respective untreated controls. GM-6001 targeted both pre-senescent and senescent MSC containing spheroids. However, targeting LOX (BAPN) and POSTN specifically blocked the increased invaded area but not the number of invading cells in case of senescent cell containing spheroids. Results are mean±s.e.m.; **P*<0.05, ***P*<0.01, ****P*<0.001 (Student's *t*-tests).

cytoskeletal tension, which both contribute to nuclear deformation and cell migration (Wu et al., 2018). This cytoskeletal structure is also dynamic, which allows cells to sense and respond to stimuli important in directing adhesion and motility (Wang et al., 2009; Lee and Kumar, 2016). Although cell adhesion molecules and focal adhesion proteins are upregulated with senescence, the adhesion complexes remain distributed throughout senescent MSCs instead of being localized to the leading edge as seen in pre-senescent MSCs (Fig. 2). This inability to polarize adhesive protrusions was associated with uniformly slower migration in both 2D and 3D systems (Figs 2 and 3; Fig. S2). However, migration of MSCs was more reduced in 3D compared to in 2D. In 3D tissue microenvironments, nuclear deformation is also essential for cell migration through pores that are often smaller than the non-deformed nucleus (Friedl et al., 2011). The nuclei of senescent MSCs are larger (feret diameter of ∼7–11 µm) than the size of collagen pores (diameter of ∼6–7 µm) (Banerjee et al., 2008). With increased collagen concentration, the cell migration will become more inhibited as pore size will decrease (Wolf et al., 2009). Reported pore sizes in normal and cancer tissues can be smaller than that of the collagen gels used in this study, albeit with a high degree of variation, and will likely further limit the migration of the senescent cells *in vivo* (Wolf et al., 2009).

Senescent MSCs continue to deposit and crosslink collagen in the surrounding matrix, but because they are less motile; this may lead to the formation of a highly dysregulated collagen network surrounding senescent cells (Fig. 3). The upregulation of MMP inhibitors (TIMPs) and crosslinking agents (transglutaminase and LOX) suggests that senescent MSCs will increase the rigidity of the surrounding matrix. The ECM proteins we found to be upregulated in senescent MSCs were also consistent with ECM alterations seen in more-invasive breast cancers (Abbott et al., 2008). High expression of these ECM proteins corresponded with reduced disease survival in patients with a basal subtype of breast cancer (Fig. S7). Among these ECM proteins, the increased expression of the matricellular protein POSTN has been associated with increased metastasis and poor survival in invasive breast cancer patients (Kim et al., 2017; Ratajczak-Wielgomas et al., 2017). It is also highly expressed in both cancer cells and CAFs from invasive ductal breast carcinomas (Ratajczak-Wielgomas et al., 2016). POSTN was upregulated in both 2D and 3D cultures of senescent MSCs, suggesting that senescent MSCs contribute to aggressive breast tumor phenotypes through the upregulation of this matricellular protein. Interestingly, other positive markers of CAFs including α-SMA, FAP and VIM are also upregulated in senescent MSCs (Tao et al., 2017).

We created a 3D matrix interface model that not only allows direct heterotypic interactions between MSCs and BCCs but also enables us to monitor both single and collective cell invasion, and surrounding matrix remodeling. MSCs and BCCs distributed in cell solution self-organized in spheroid cultures, with MSCs at the core and BCCs at the periphery. Over time, pre-senescent MSCs migrated out of the core and were more equally distributed throughout these cultures; however, senescent MSCs remained at the spheroid core, structurally supporting the spheroid growth and secreting ECM proteins to remodel the surrounding matrix. This spontaneous reorganization of mixed cell populations into aggregates of similar cells has been demonstrated in co-cultures of invasive and non-invasive breast cancer cells (Oswald et al., 2017) and embryonic tissues (Amack and Manning, 2012), and is thought to be mediated by homotypic or heterotypic cadherin interactions (McAndrews et al., 2015a). While cadherin-mediated interactions can drive the initial sorting, the reduced motility of senescent MSCs is likely responsible for keeping these cells at the spheroid core. Our

Journal of Cell Science (2020) 133, jcs232470. doi:10.1242/jcs.232470

mosaic confocal images demonstrated that spheroids formed from senescent MSCs are tightly packed, in part due to the high number of senescent MSCs that remain viable at the spheroid core (Fig. S5). By analyzing mosaics of confocal images, it became increasingly clear that changes in cellular shape from core to the periphery of the spheroids is highest for spheroids formed with senescent MSCs (Fig. S6). Cells at the periphery were more elongated with fewer cell–cell contacts and higher variation in cell shape factors; this is in contrast to cells at the core, which were tightly packed into circular shapes with reduced variation in cell shape, akin to a jammed state (Dolega et al., 2017; Oswald et al., 2017). This distribution of cell shape is consistent with high solid stress at the core and cells at the perimeter transitioning to a more-invasive cancer cell phenotype. Conversely, pre-senescent MSCs maintained their highly motile phenotype and rapidly moved into the surrounding collagen gel leaving a hollow core behind, suggesting that cells remaining at the core of these spheroids would reside in a relatively unjammed state. Haeger et al. have shown that the jammed state in confined tissue (e.g. densely packed group of cells in tracks created by leader cells) promotes collective invasion of mesenchymal tumor (Haeger et al., 2014). In our model, tracks created by migrating pre-senescent MSCs can be used by jammed BCCs and senescent cells to allow collective invasion.

Other studies have demonstrated that fibroblast remodeling of the matrix generates tracks for cancer cells to follow, promoting cancer cell invasion and metastasis (Gaggioli et al., 2007). The coefficient of alignment of the surrounding collagen for pre-senescent MSC spheroid was very similar to the alignment coefficient of individual pre-senescent MSCs in collagen (Figs 4 and 6). The senescent MSCs remained at the core and were not able to directly affect the collagen surrounding the spheroid surface, which was dominated by alignment with BCCs. Although senescent MSCs were unable to move into the surrounding matrix, they clearly induced a more-proliferative and invasive phenotype in BCCs compared to pre-senescent MSCs. Furthermore, the invasive behavior was enhanced when BCCs were combined with a mixture of pre-senescent and senescent MSCs. This result can be attributed to the matrix remodeling and soluble factor secretion effects of senescent MSCs, which enhanced the migration of pre-senescent MSCs allowing them to form tracks in the collagen network for cancer cells to follow. Together, these results suggest that a mixed population of MSCs can synergistically combine the invading properties of pre-senescent MSCs and SASP/ECM-remodeling properties of senescent MSCs to facilitate BCC invasion. This is significant because senescent MSCs are likely a small population of stromal cells *in vivo*. However, senescent MSCs can 'transfer' senescence to other stromal cells through paracrine signaling (Severino et al., 2013).

In summary, we have demonstrated that senescent MSCs that accumulate in tumors alter the local and bulk mechanical properties of tissue ECM to promote more-invasive breast cancer phenotypes. Understanding the interactions between senescent stromal cells and cancer cells is critical in developing new strategies for targeting age-associated cancer progression. Although these studies focused on MSCs in breast cancers, senescence-induced biophysical changes in MSCs would apply to other age-associated fibrotic diseases.

MATERIALS AND METHODS

Cell culture

Human bone marrow-derived MSCs (MSCs) isolated from a healthy 24-year-old female donor (8001 L) were obtained from Texas A&M Cell Distribution Center. MSCs were cultured in Minimum Essential Medium Alpha (αMEM; Corning) supplemented with 20% fetal bovine serum (FBS, Atlanta Biologicals, lot #J15102), 15 mM HEPES (Fisher Chemicals), 1% penicillin-streptomycin (Corning) and 1% L-glutamine (Corning). MSCs were used between passage 2 and 6. The triple-negative human BCC line MDA-MB-231 was purchased from the ATCC and cultured in DMEM and Ham's F12 mix (Corning) supplemented with 10% FBS and 1% penicillin-streptomycin. All cells were maintained at 37° C and 5% carbon dioxide as per supplier's instructions.

Irradiation

MSCs cultured to 60% confluence were exposed to 15 Gy γ-irradiation using a Mark I 68A137Cs Irradiator at a rate of 5.04 Gy/min for 3 min. After 10 days, MSCs were assessed to confirm senescence and were subsequently used for all experiments. This model of induced senescence was selected to allow for direct comparison between pre- senescent and senescent MSCs from the same donor with large numbers of cells.

Proliferation

MSCs were cultured on glass coverslips and incubated overnight (12 h) with 10 µM bromodeoxyuridine (BrdU) (Millipore Sigma). Cells were then fixed in 4% formaldehyde followed by permeabilization with 0.5% Triton X-100 in PBS. After treatment with 4 M HCl, cells were blocked with 5% horse serum. Following sequential incubation with biotinylated anti-BrdU (Biolegend) primary antibody (cat. no. 339810, 1:100) and DyLight™ 488 Streptavidin (cat. no. 405218, Biolegend) which binds to biotin with high affinity, the coverslips were sealed with VectaShield Mounting Medium with propidium iodide (PI) (Vector Labs) and imaged on Nikon Eclipse Ti inverted microscope at 20× magnification. For quantification, the number of BrdU-positive cells (green nuclei) were normalized to the total number of cells (red nuclei).

Cell and nuclear morphology

Pre-senescent and senescent MSCs were cultured in a 24-well plate and were subsequently fixed with ice-cold methanol followed by staining with Crystal Violet (10 mg/ml; Carolina Biological) and DAPI (10 µg/ml; Acros Organics). To analyze cell morphology, cell boundaries were manually traced in ImageJ (n>1000 cells per condition). For quantitative analysis of the nuclear area, we used automated processing of the images (n>1000 cells per condition) through CellProfiler (Broad Institute).

Immunostaining of cytoskeleton

To visualize filamentous actin and focal adhesion protein vinculin, we followed the previously described immunostaining protocol (McGrail et al., 2012). Briefly, MSCs cultured on glass coverslips were fixed with 4% formaldehyde, permeabilized with Triton X-100 (0.5%) and blocked with 5% horse serum. Cells were then incubated in anti-vinculin antibody (1:100, cat. no. 700062, Invitrogen) primary antibody followed by staining with TRITC-conjugated Phalloidin (Cytoskeleton Inc.), and Alexa Fluor 488-conjugated anti-rabbit IgG (H+L) secondary antibody (cat. no. A32731, Invitrogen). Finally, samples were sealed with Vectashield Mounting Medium with DAPI. High-resolution images taken with Nikon Eclipse Ti microscope were used to analyze actin stress fibers with CT-FIRE (LOCI). Focal adhesion size and distance were processed through a custom pipeline in CellProfiler (Broad Institute). Images were thresholded and segmented using the IdentifyPrimaryObjects module. Focal adhesion area was measured using MeasureObjectSizeShape and distance was measured with RelateObjects. The centroid and minimum sub-parameter were used to measure focal adhesion distance from the centroid and edge of the cell, respectively.

Multiple particle tracking

To quantify differences in intracellular mechanics, the thermal motion of ballistically injected 200 nm green fluorescent particles embedded in cytosol was tracked in live cells based on our previously established protocols (McGrail et al., 2012; Ghosh et al., 2014). Videos of particle motion were taken at 30 frames per second for 20 s using a Nikon Eclipse Ti inverted microscope and QuantEM CCD camera. Particle displacements were tracked in MATLAB, based on previous established algorithms

Journal of Cell Science (2020) 133, jcs232470. doi:10.1242/jcs.232470

(McGrail et al., 2013). Briefly, a band-pass filter is used to identify particles based on intensity-weighted centroids, then a Hungarian linker algorithm is used to determine traces of particle motion, and the time-dependent 2D particle mean squared displacements (MSDs) are calculated from particle motion as $<\Delta r^2(\Delta t)>=<[x(t+\Delta t)-x(t)]^2+[y(t+\Delta t)-y(t)]^2>$. For each condition an average of 15 cells with 10–20 particles per cell were analyzed for more than 200 particles per condition.

Nuclear tracking

To quantify nuclear mechanics, MSCs seeded on collagen-coated glass were labeled with Hoechst 33342 (cat. no. 62249, Invitrogen). Using techniques described above for MPT, the motion of Hoechst-labeled chromatin was tracked, and the relaxation time (characterizing the transition from elastic to viscous behavior) was determined from the logarithmic slope of the MSD (McGrail et al., 2015).

Cell motility

MSCs were seeded on collagen-coated 24-well plates at sub-confluent density. Cells were labeled with Hoechst 33342 live-cell dye (cat. no. 62249, Invitrogen) according to the manufacturer's instructions and then imaged on a Nikon Eclipse Ti inverted microscope equipped with an environmental chamber and maintained at 37°C and 5% carbon dioxide throughout the experiment. Images were captured every 10 min for up to 12 h. Image stacks were processed in MATLAB to track the *xy* coordinates of cell nuclei to determine cell velocity (McGrail et al., 2015).

qRT-PCR analysis

All the reagents used for RNA isolation, cDNA synthesis and qRT-PCR were purchased from Bio-Rad. Total mRNA was extracted from the MSCs with PureZOL RNA isolation reagent according to the manufacturer's protocol. The purity and integrity of the RNA was assessed using Nanodrop 1000, and subsequently cDNA was synthesized using iScript cDNA synthesis kit. 1 µg of RNA was converted into cDNA followed by real-time PCR for senescence markers. Primers used were as follows: *APO1*: forward, 5′-CAAATGTCTATCCACAGGCTAACCC-3′; and reverse, 5′-AGAGGTAATTTAGAGGCAAAGTGGC-3′; *P16*: forward, 5′-CACTCACGCCCTAAGC-3′ and reverse, 5′-GCAGTGTGACTCAAGAGAA-3′; *IL6*: forward, 5′-CCAGGAGCCCAGCTATGAAC-3′ and reverse, 5′-CCCAGGGAGAAGGCAACTG-3′; *IL8*: forward, 5′-GAGTGGACCACACTGCGCCA-3′ and reverse: 5′-TCCACAACCCTCTGCACCCAGT-3′; *IL1β*: forward, 5′-TGCACGCTCCGGGACTCACA-3′ and reverse, 5′-CATGGAGAACACCACTTGTTGCTCC-3′; *18s*: forward, 5′-CGCCGCTAGAGGTGAAATTC-3′ and reverse: 5′-TTGGCAAATGCTTTCGCTC-3′.

Proteome analysis

Pre-senescent and senescent MSCs cultured in T-175 flasks were trypsinized and centrifuged at 700 ***g*** for 10 min to pellet the cells. Cell pellets were suspended in 30 µl PBS and flash frozen in liquid nitrogen before transferring on dry ice to Brown University's Proteomics Core Facility for protein analysis (n=4). To select peptides that show a statistically significant change in abundance between pre-senescent and senescent MSCs, q-values for multiple hypothesis tests were calculated based on P-values from two-tailed unpaired Student's t-tests using the R package QVALUE. The values reported here are the log2-transformed fold change in senescent MSCs compared to pre-senescent MSCs.

Pathway analysis

Pathway analysis and visualization was carried out using web based-tool Metaboanalyst 3.0 using the KEGG (www.genome.jp/kegg/) pathway database (Chong et al., 2018). Significantly regulated peptides from proteomic analysis were used separately to identify most significantly regulated pathways.

3D collagen gels

Pre-senescent and senescent MSCs were harvested and suspended in collagen I (Corning) solution at final concentration of 1.5 mg/ml and plated on a 96-well plate as per previous protocol (McAndrews et al., 2015a,b). Collagen gels were polymerized on ice for 45 min followed by incubation in 37°C for 2 h. After adding medium, gels were immediately moved to the microscope to capture images every 15 min for up to 12 h. The number of protrusions were manually analyzed using FIJI (ImageJ). Image stacks were processed in MATLAB to track the *xy* coordinates of cell nuclei to determine cell velocity (McGrail et al., 2015).

Matrix interface model

GFP-positive MDA-MB-231 cells were mixed at an equal ratio with three groups of MSCs – pre-senescent, senescent, or 1:1 mixture of pre-senescent and senescent MSCs. Then, the cell solutions were seeded on top of an agarose-coated 96-well plate at a density of 2000 cells/well to stimulate cell aggregate formation in DMEM/F12 medium supplemented with 10% FBS and 1% penicillin and streptomycin. Cell aggregates were harvested after 72 h and spun down briefly to recollect them in serum-free medium. Aggregates were then suspended in collagen I (Corning) solution at final concentration of 1.5 mg/ml and plated on a 96 well-plate as per previous protocol (McAndrews et al., 2015a,b). Collagen gels were polymerized on ice for 45 min followed by incubation in 37°C for 2 h. After adding medium, gels were immediately moved to the microscope to capture images every 10 min for up to 16 h. Spheroid area, cell numbers and cell distance from spheroid boundary were manually analyzed in Nikon elements software. The number of protrusions was calculated using temporal analysis of spheroid imaging (TASI) (Hou et al., 2018).

SHG imaging of collagen gels

Multiphoton microscopy was used to image 3D collagen gels by SHG (Perentes et al., 2009); collagen fibers are an efficient source of SHG in part to their crystalline structure, and multiphoton microscopy can be used for simultaneous imaging of collagen (by SHG) and MSCs (stained with NucRed). Spheroids embedded in collagen gels for 16 h were fixed in 4% formaldehyde and incubated with NucRed; after washing with PBS, collagen gels were immobilized using an agarose mold before mounting on coverslips. Olympus multiphoton microscope with 810 nm excitation and 405 nm emission filters and a 25× water immersion lens was used to obtain 3D image stacks (up to 100 µm thick with 1 µm separation distance). Multiple parameters were quantified for each slice of the acquired stack using CurveAlign4.0 (Bredfeldt et al., 2014). Here, we analyzed the coefficient of alignment based on the orientation of collagen fibers in an image. For single-cell analysis, cell boundaries were traced manually and a uniform outward dilation of 50 µm along the cell outline was used to determine the local fiber properties surrounding the cells, including the coefficient of alignment and density. For spheroid image stacks, alignment and density were calculated for uniform size boxes (locally) and over the entire image. Additionally, the CT-FIRE module was used to measure fiber properties, including the length and width for the collagen around spheroids.

Inhibitor studies

BCC spheroids with the mixed population of pre-senescent and senescent MSCs were treated with inhibitors. Small-molecule inhibitor and antibody stocks were prepared in dimethyl sulfoxide (DMSO) and PBS, respectively. All inhibitors were further diluted to the final concentration in serum-free medium. To disrupt ECM reorganization the following inhibitors were used: pan-MMP inhibitor GM-6001(20 µM; Cayman Chemicals), LOX inhibitor β-aminopropionitrile (BAPN; 20 µM; Cayman Chemicals), and anti-POSTN antibody (2.5 µg/ml, 200 µl; cat. no. SAB4200197, Sigma-Aldrich).

Statistics

All assays were performed with minimum of three replicates and the results are reported here as mean±s.e.m. or in box or volin plots. Student's t-test was utilized for comparison between groups with $P<0.05$ considered as significant (*$P<0.05$, **$P<0.01$, ***$P<0.001$).

Acknowledgements

We would like to thank Genomics and Proteomics core facility for their support and expertise, and especially Dr Nagib Ahsan.

Competing interests
The authors declare no competing or financial interests.

Author contributions
Conceptualization: D.G., M.R.D.; Methodology: D.G., C.M.-P., N.Q.; Software: D.G., C.M.-P., N.Q., B.X.; Validation: D.G., C.M.-P., N.Q., B.X., A.H.L.; Formal analysis: D.G., N.Q., B.X., A.H.L.; Investigation: D.G., C.M.-P., N.Q.; Resources: M.R.D.; Data curation: D.G., C.M.-P., N.Q., B.X., A.H.L.; Writing - original draft: D.G., M.R.D.; Writing - review & editing: D.G., M.R.D.; Visualization: D.G., C.M.-P., N.Q.; Supervision: M.R.D.; Project administration: M.R.D.; Funding acquisition: M.R.D.

Funding
This work was funded by grants from the National Science Foundation (1825174), the National Institutes of Health NIGMS (P30 GM110750) and by a National Science Foundation Graduate Research Fellowship to C.M.P. and T32 grant (HL134625) to N.Q. Deposited in PMC for release after 12 months.

Supplementary information
Supplementary information available online at
http://jcs.biologists.org/lookup/doi/10.1242/jcs.232470.supplemental

References

Abbott, K. L., Aoki, K., Lim, J.-M., Porterfield, M., Johnson, R., O'Regan, R. M., Wells, L., Tiemeyer, M. and Pierce, M. (2008). Targeted glycoproteomic identification of biomarkers for human breast carcinoma. *J. Proteome Res.* **7**, 1470-1480. doi:10.1021/pr700792g

Acosta, J. C., Banito, A., Wuestefeld, T., Georgilis, A., Janich, P., Morton, J. P., Athineos, D., Kang, T.-W., Lasitschka, F., Andrulis, M. et al. (2013). A complex secretory program orchestrated by the inflammasome controls paracrine senescence. *Nat. Cell Biol.* **15**, 978-990. doi:10.1038/ncb2784

Aifuwa, I., Giri, A., Longe, N., Lee, S. H., An, S. S. and Wirtz, D. (2015). Senescent stromal cells induce cancer cell migration via inhibition of RhoA/ROCK/myosin-based cell contractility. *Oncotarget* **6**, 30516-30531. doi:10.18632/oncotarget.5854

Alessio, N., Del Gaudio, S., Capasso, S., Di Bernardo, G., Cappabianca, S., Cipollaro, M., Peluso, G. and Galderisi, U. (2015). Low dose radiation induced senescence of human mesenchymal stromal cells and impaired the autophagy process. *Oncotarget* **6**, 8155-8166. doi:10.18632/oncotarget.2692

Amack, J. D. and Manning, M. L. (2012). Knowing the boundaries: extending the differential adhesion hypothesis in embryonic cell sorting. *Science* **338**, 212-215. doi:10.1126/science.1223953

Banerjee, P., Lenz, D., Robinson, J. P., Rickus, J. L. and Bhunia, A. K. (2008). A novel and simple cell-based detection system with a collagen-encapsulated B-lymphocyte cell line as a biosensor for rapid detection of pathogens and toxins. *Lab. Investig.* **88**, 196-206. doi:10.1038/labinvest.3700703

Bartosh, T. J., Ullah, M., Zeitouni, S., Beaver, J. and Prockop, D. J. (2016). Cancer cells enter dormancy after cannibalizing mesenchymal stem/stromal cells (MSCs). *Proc. Natl Acad. Sci. USA* **113**, E6447-E6456. doi:10.1073/pnas.1612290113

Bredfeldt, J. S., Liu, Y., Pehlke, C. A., Conklin, M. W., Szulczewski, J. M., Inman, D. R., Keely, P. J., Nowak, R. D., Mackie, T. R. and Eliceiri, K. W. et al. (2014). Computational segmentation of collagen fibers from second-harmonic generation images of breast cancer. *J. Biomed. Opt.* **19**, 16007. doi:10.1117/1.JBO.19.1.016007

Calvo, F., Ege, N., Grande-Garcia, A., Hooper, S., Jenkins, R. P., Chaudhry, S. I., Harrington, K., Williamson, P., Moeendarbary, E., Charras, G. et al. (2013). Mechanotransduction and YAP-dependent matrix remodelling is required for the generation and maintenance of cancer-associated fibroblasts. *Nat. Cell Biol.* **15**, 637-646. doi:10.1038/ncb2756

Campisi, J. (2013). Aging, cellular senescence, and cancer. *Ann. Rev. Physiol.* **75**, 685-705. doi:10.1146/annurev-physiol-030212-183653

Caplan, A. I. and Dennis, J. E. (2006). Mesenchymal stem cells as trophic mediators. *J. Cell. Biochem.* 1076-1084. doi:10.1002/jcb.20886

Cárdenes, N., Ãlvarez, D., Sellarés, J., Peng, Y., Corey, C., Wecht, S., Nouraie, S. M., Shanker, S., Sembrat, J., Bueno, M. et al. (2018). Senescence of bone marrow-derived mesenchymal stem cells from patients with idiopathic pulmonary fibrosis. *Stem Cell Res. Ther.* **9**, 257. doi:10.1186/s13287-018-0970-6

Carey, S. P., Martin, K. E. and Reinhart-King, C. A. (2017). Three-dimensional collagen matrix induces a mechanosensitive invasive epithelial phenotype. *Sci. Rep.* **7**, 42088. doi:10.1038/srep42088

Chong, J., Soufan, O., Li, C., Caraus, I., Li, S., Bourque, G., Wishart, D. S. and Xia, J. (2018). MetaboAnalyst 4.0: towards more transparent and integrative metabolomics analysis. *Nucleic Acids Res.* **46**, W486-W494. doi:10.1093/nar/gky310

Criscione, S. W., Teo, Y. V. and Neretti, N. (2016). The chromatin landscape of cellular senescence. *Trends Genet.* **32**, 751-761. doi:10.1016/j.tig.2016.09.005

Dahl, K. N., Scaffidi, P., Islam, M. F., Yodh, A. G., Wilson, K. L. and Misteli, T. (2006). Distinct structural and mechanical properties of the nuclear lamina in Hutchinson-Gilford progeria syndrome. *Proc. Natl Acad. Sci. USA* **103**, 10271-10276. doi:10.1073/pnas.0601058103

Dawson, M. R., Tseng, Y., Lee, J. and McAndrews, K. (2014). Intracellular particle tracking microrheology. *Handbook of Imaging in Biological Mechanics* **310**, 381-388. doi:10.1201/b17566-40

De Araújo Farias, V., O'Valle, F., Lerma, B. A., Ruiz de Almodóvar, C., López-Peñalver, J. J., Nieto, A., Santos, A., Fernández, B. I., Guerra-Librero, A. and Ruiz-Ruiz, M. C. (2015). Human mesenchymal stem cells enhance the systemic effects of radiotherapy. *Oncotarget* **6**, 31164-31180. doi:10.18632/oncotarget.5216

Dolega, M. E., Delarue, M., Ingremeau, F., Prost, J., Delon, A. and Cappello, G. (2017). Cell-like pressure sensors reveal increase of mechanical stress towards the core of multicellular spheroids under compression. *Nat. Commun.* **8**, 14056. doi:10.1038/ncomms14056

Fehrer, C. and Lepperdinger, G. (2005). Mesenchymal stem cell aging. *Exp. Gerontol.* **40**, 926-930. doi:10.1016/j.exger.2005.07.006

Ferrera, D., Canale, C., Marotta, R., Mazzaro, N., Gritti, M., Mazzanti, M., Capellari, S., Cortelli, P. and Gasparini, L. (2014). Lamin B1 overexpression increases nuclear rigidity in autosomal dominant leukodystrophy fibroblasts. *FASEB J.* **28**, 3906-3918. doi:10.1096/fj.13-247635

Frantz, C., Stewart, K. M. and Weaver, V. M. (2010). The extracellular matrix at a glance. *J. Cell Sci.* **123**, 4195-4200. doi:10.1242/jcs.023820

Friedl, P., Wolf, K. and Lammerding, J. (2011). Nuclear mechanics during cell migration. *Curr. Opin. Cell Biol.* **23**, 55-64. doi:10.1016/j.ceb.2010.10.015

Gaggioli, C., Hooper, S., Hidalgo-Carcedo, C., Grosse, R., Marshall, J. F., Harrington, K. and Sahai, E. (2007). Fibroblast-led collective invasion of carcinoma cells with differing roles for RhoGTPases in leading and following cells. *Nat. Cell Biol.* **9**, 1392-1400. doi:10.1038/ncb1658

Ghosh, D., Lili, L., Mcgrail, D. J., Matyunina, L. V., Mcdonald, J. F. and Dawson, M. R. (2014). Integral role of platelet-derived growth factor in mediating transforming growth factor-β1-dependent mesenchymal stem cell stiffening. *Stem Cells Dev.* **23**, 245-261. doi:10.1089/scd.2013.0240

Gruenbaum, Y. and Foisner, R. (2015). Lamins: nuclear intermediate filament proteins with fundamental functions in nuclear mechanics and genome regulation. *Annu. Rev. Biochem.* **84**, 131-164. doi:10.1146/annurev-biochem-060614-034115

Haeger, A., Krause, M., Wolf, K. and Friedl, P. (2014). Cell jamming: collective invasion of mesenchymal tumor cells imposed by tissue confinement. *Biochim. Biophys. Acta* **1840**, 2386-2395. doi:10.1016/j.bbagen.2014.03.020

Harada, T., Swift, J., Irianto, J., Shin, J.-W., Spinler, K. R., Athirasala, A., Diegmiller, R., Dingal, P. C. D. P., Ivanovska, I. L. and Discher, D. E. (2014). Nuclear lamin stiffness is a barrier to 3D migration, but softness can limit survival. *J. Cell Biol.* **204**, 669-682. doi:10.1083/jcb.201308029

Ho, I. A. W., Toh, H. C., Ng, W. H., Teo, Y. L., Guo, C. M., Hui, K. M. and Lam, P. Y. P. (2013). Human bone marrow-derived mesenchymal stem cells suppress human glioma growth through inhibition of angiogenesis. *Stem Cells*, **31**, 146-155. doi:10.1002/stem.1247

Hou, Y., Konen, J., Brat, D. J., Marcus, A. I. and Cooper, L. A. D. (2018). TASI: a software tool for spatial-temporal quantification of tumor spheroid dynamics. *Sci. Rep.* **8**, 7248. doi:10.1038/s41598-018-25337-4

Kadota, T., Fujita, Y., Yoshioka, Y., Araya, J., Kuwano, K. and Ochiya, T. (2018). Emerging role of extracellular vesicles as a senescence-associated secretory phenotype: Insights into the pathophysiology of lung diseases. *Mol. Asp. Med.* **60**, 92-103. doi:10.1016/j.mam.2017.11.005

Kalluri, R. and Zeisberg, M. (2006). Fibroblasts in cancer. *Nat. Rev. Cancer* **6**, 392-401. doi:10.1038/nrc1877

Karnoub, A. E., Dash, A. B., Vo, A. P., Sullivan, A., Brooks, M. W., Bell, G. W., Richardson, A. L., Polyak, K., Tubo, R. and Weinberg, R. A. (2007). Mesenchymal stem cells within tumour stroma promote breast cancer metastasis. *Nature* **449**, 557-563. doi:10.1038/nature06188

Kasper, G., Mao, L., Geissler, S., Draycheva, A., Trippens, J., Kühnisch, J., Tschirschmann, M., Kaspar, K., Perka, C., Duda, G. N. et al. (2009). Insights into mesenchymal stem cell aging: involvement of antioxidant defense and actin cytoskeleton. *Stem Cells* **27**, 1288-1297. doi:10.1002/stem.49

Kim, G.-E., Lee, J. S., Park, M. H. and Yoon, J. H. (2017). Epithelial periostin expression is correlated with poor survival in patients with invasive breast carcinoma. *PLoS ONE* **12**, e0187635. doi:10.1371/journal.pone.0187635

Kole, T. P., Tseng Y, Jiang I, Katz JL, Wirtz D. (2005). Intracellular mechanics of migrating fibroblasts. *Biophys. J.* **16**, 328-338. doi:10.1091/mbc.e04-06-0485

Krtolica, A., Parrinello, S., Lockett, S., Desprez, P.-Y. and Campisi, J. (2001). Senescent fibroblasts promote epithelial cell growth and tumorigenesis: a link between cancer and aging. *Proc. Natl. Acad. Sci. USA* **98**, 12072-12077. doi:10.1073/pnas.211053698

Kümper, S. and Marshall, C. J. (2011). ROCK-driven actomyosin contractility induces tissue stiffness and tumor growth. *Cancer Cell* **19**, 695-697. doi:10.1016/j.ccr.2011.05.021

Lacerda, L., Debeb, B. G., Smith, D., Larson, R., Solley, T., Xu, W., Krishnamurthy, S., Gong, Y., Levy, L. B., Buchholz, T. et al. (2015). Mesenchymal stem cells mediate the clinical phenotype of inflammatory breast cancer in a preclinical model. *Breast Cancer Res.* **17**, 42. doi:10.1186/s13058-015-0549-4

Lee, S. and Kumar, S. (2016). Actomyosin stress fiber mechanosensing in 2D and 3D. *F1000Research* **5**, 2261. doi:10.12688/f1000research.8800.1

Lehmann, B. D., Paine, M. S., Brooks, A. M., Mccubrey, J. A., Renegar, R. H., Wang, R. and Terrian, D. M. (2008). Senescence-associated exosome release from human prostate cancer cells. *Cancer Res.* **68**, 7864-7871. doi:10.1158/0008-5472.CAN-07-6538

Lele, T. P., Dickinson, R. B. and Gundersen, G. G. (2018). Mechanical principles of nuclear shaping and positioning. *J. Cell Biol.* **217**, 3330-3342. doi:10.1083/jcb.201804052

Levental, K. R., Yu, H., Kass, L., Lakins, J. N., Egeblad, M., Erler, J. T., Fong, S. F., Csiszar, K., Giaccia, A., Weninger, W. et al. (2009). Matrix crosslinking forces tumor progression by enhancing integrin signaling. *Cell* **139**, 891-906. doi:10.1016/j.cell.2009.10.027

Liu, D. and Hornsby, P. J. (2007). Senescent human fibroblasts increase the early growth of xenograft tumors via matrix metalloproteinase secretion. *Cancer Res.* **67**, 3117-3126. doi:10.1158/0008-5472.CAN-06-3452

Lunyak, V. V., Amaro-Ortiz, A. and Gaur, M. (2017). Mesenchymal stem cells secretory responses: senescence messaging secretome and immunomodulation perspective. *Front. Genet.* **8**, 220. doi:10.3389/fgene.2017.00220

Luo, H., Tu, G., Liu, Z. and Liu, M. (2015). Cancer-associated fibroblasts: a multifaceted driver of breast cancer progression. *Cancer Lett.* **361**, 155-163. doi:10.1016/j.canlet.2015.02.018

Marthandan, S., Menzel, U., Priebe, S., Groth, M., Guthke, R., Platzer, M., Hemmerich, P., Kaether, C. and Diekmann, S. (2016). Conserved genes and pathways in primary human fibroblast strains undergoing replicative and radiation induced senescence. *Biol. Res.* **49**, 34. doi:10.1186/s40659-016-0095-2

Mathon, N. F. and Lloyd, A. C. (2001). Cell senescence and cancer. *Nat. Rev. Cancer* **1**, 203-213. doi:10.1038/35106045

McAndrews, K. M., Yi, J., Mcgrail, D. J. and Dawson, M. R. (2015a). Enhanced adhesion of stromal cells to invasive cancer cells regulated by cadherin 11. *ACS Chem. Biol.* **10**, 1932-1938. doi:10.1021/acschembio.5b00353

McAndrews, K. M., McGrail, D. J., Ravikumar, N. and Dawson, M. R. (2015b). Mesenchymal stem cells induce directional migration of invasive breast cancer cells through TGF-β. *Sci. Rep.* **5**, 16941. doi:10.1038/srep16941

McGrail, D. J., Ghosh, D., Quach, N. D. and Dawson, M. R. (2012). Differential mechanical response of mesenchymal stem cells and fibroblasts to tumor-secreted soluble factors. *PLoS ONE* **7**, e33248-e33248. doi:10.1371/journal.pone.0033248

McGrail, D. J., Mezencev, R., Kieu, Q. M. N., McDonald, J. F. and Dawson, M. R. (2015). SNAIL-induced epithelial-to-mesenchymal transition produces concerted biophysical changes from altered cytoskeletal gene expression. *FASEB J.* **29**, 1280-1289. doi:10.1096/fj.14-257345

McGrail, D. J., McAndrews, K. M. and Dawson, M. R. (2013). Biomechanical analysis predicts decreased human mesenchymal stem cell function before molecular differences. *Exp. Cell Res.* **319**, 684-696. doi:10.1016/j.yexcr.2012.11.017

McLean, K., Gong, Y., Choi, Y., Deng, N., Yang, K., Bai, S., Cabrera, L., Keller, E., McCauley, L., Cho, K. R. et al. (2011). Human ovarian carcinoma-associated mesenchymal stem cells regulate cancer stem cells and tumorigenesis via altered BMP production. *J. Clin. Investig.* **121**, 3206-3219. doi:10.1172/JCI45273

Mishra, P. J., Mishra, P. J., Humeniuk, R., Medina, D. J., Alexe, G., Mesirov, J. P., Ganesan, S., Glod, J. W. and Banerjee, D. (2008). Carcinoma-associated fibroblast-like differentiation of human mesenchymal stem cells. *Cancer Res.* **68**, 4331-4339. doi:10.1158/0008-5472.CAN-08-0943

Muñoz-Espín, D. and Serrano, M. (2014). Cellular senescence: from physiology to pathology. *Nat. Rev. Mol. Cell Biol.* **15**, 482-496. doi:10.1038/nrm3823

O'Malley, G., Heijltjes, M., Houston, A. M., Rani, S., Ritter, T., Egan, L. J. and Ryan, A. E. (2016). Mesenchymal stromal cells (MSCs) and colorectal cancer: a troublesome twosome for the anti-tumour immune response? *Oncotarget* **7**, 60752-60774. doi:10.18632/oncotarget.11354

Orimo, A., Gupta, P. B., Sgroi, D. C., Arenzana-Seisdedos, F., Delaunay, T., Naeem, R., Carey, V. J., Richardson, A. L. and Weinberg, R. A. (2005). Stromal fibroblasts present in invasive human breast carcinomas promote tumor growth and angiogenesis through elevated SDF-1/CXCL12 secretion. *Cell* **121**, 335-348. doi:10.1016/j.cell.2005.02.034

Ortiz-Montero, P., Londoño-Vallejo, A. and Vernot, J.-P. (2017). Senescence-associated IL-6 and IL-8 cytokines induce a self- and cross-reinforced senescence/inflammatory milieu strengthening tumorigenic capabilities in the MCF-7 breast cancer cell line. *Cell Commun. Signal.* **15**, 17. doi:10.1186/s12964-017-0172-3

Oswald, L., Grosser, S., Smith, D. M. and Käs, J. A. (2017). Jamming transitions in cancer. *J. Phys. D Appl. Phys.* **50**, 483001. doi:10.1088/1361-6463/aa8e83

Parrinello, S., Coppe, J. P., Krtolica, A. and Campisi, J. (2005). Stromal-epithelial interactions in aging and cancer: senescent fibroblasts alter epithelial cell differentiation. *J. Cell Sci.* **118**, 485-496. doi:10.1242/jcs.01635

Paszek, M. J., Zahir, N., Johnson, K. R., Lakins, J. N., Rozenberg, G. I., Gefen, A., Reinhart-King, C. A., Margulies, S. S., Dembo, M., Boettiger, D. et al. (2005). Tensional homeostasis and the malignant phenotype. *Cancer Cell* **8**, 241-254. doi:10.1016/j.ccr.2005.08.010

Perentes, J. Y., McKee, T. D., Ley, C. D., Mathiew, H., Dawson, M., Padera, T. P., Munn, L. L., Jain, R. K. and Boucher, Y. (2009). In vivo imaging of extracellular matrix remodeling by tumor- associated fibroblasts. *Nat. Methods* **6**, 143-145. doi:10.1038/nmeth.1295

Phillip, J. M., Aifuwa, I., Walston, J. and Wirtz, D. (2015). The mechanobiology of aging. *Annu. Rev. Biomed. Eng.* **17**, 113-141. doi:10.1146/annurev-bioeng-071114-040829

Ratajczak-Wielgomas, K., Grzegrzolka, J., Piotrowska, A., Gomulkiewicz, A., Witkiewicz, W. and Dziegiel, P. (2016). Periostin expression in cancer-associated fibroblasts of invasive ductal breast carcinoma. *Oncol. Rep.* **36**, 2745-2754. doi:10.3892/or.2016.5095

Ratajczak-Wielgomas, K., Grzegrzolka, J., Piotrowska, A., Matkowski, R., Wojnar, A., Rys, J., Ugorski, M. and Dziegiel, P. (2017). Expression of periostin in breast cancer cells. *Int. J. Oncol.* **51**, 1300-1310. doi:10.3892/ijo.2017.4109

Rodier, F. and Campisi, J. (2011). Four faces of cellular senescence. *J. Cell Biol.* **192**, 547-556. doi:10.1083/jcb.201009094

Severino, V., Alessio, N., Farina, A., Sandomenico, A., Cipollaro, M., Peluso, G., Galderisi, U. and Chambery, A. (2013). Insulin-like growth factor binding proteins 4 and 7 released by senescent cells promote premature senescence in mesenchymal stem cells. *Cell Death Dis.* **4**, e911. doi:10.1038/cddis.2013.445

Shangguan, L., Ti, X., Krause, U., Hai, B., Zhao, Y., Yang, Z. and Liu, F. (2012). Inhibition of TGF-β/Smad signaling by BAMBI blocks differentiation of human mesenchymal stem cells to carcinoma-associated fibroblasts and abolishes their protumor effects. *Stem Cells* **30**, 2810-2819. doi:10.1002/stem.1251

Stearns-Reider, K. M., D'Amore, A., Beezhold, K., Rothrauff, B., Cavalli, L., Wagner, W. R., Vorp, D. A., Tsamis, A., Shinde, S., Zhang, C. et al. (2017). Aging of the skeletal muscle extracellular matrix drives a stem cell fibrogenic conversion. *Aging Cell* **16**, 518-528. doi:10.1111/acel.12578

Stephens, A. D., Banigan, E. J., Adam, S. A., Goldman, R. D. and Marko, J. F. (2017). Chromatin and lamin A determine two different mechanical response regimes of the cell nucleus. *Mol. Biol. Cell* **28**, 1984-1996. doi:10.1091/mbc.e16-09-0653

Studeny, M., Marini, F. C., Champlin, R. E., Zompetta, C., Fidler, I. J. and Andreeff, M. (2002). Bone marrow-derived mesenchymal stem cells as vehicles for interferon-beta delivery into tumors. *Cancer Res.* **62**, 3603-3608.

Swanson, E. C., Rapkin, L. M., Bazett-Jones, D. P. and Lawrence, J. B. (2015). Unfolding the story of chromatin organization in senescent cells. *Nucleus* **6**, 254-260. doi:10.1080/19491034.2015.1057670

Swift, J., Ivanovska, I. L., Buxboim, A., Harada, T., Dingal, P. C., Pinter, J., Pajerowski, J. D., Spinler, K. R., Shin, J. W., Tewari, M. et al. (2013). Nuclear lamin-a scales with tissue stiffness and enhances matrix-directed differentiation. *Science* **341**, 1240104. doi:10.1126/science.1240104

Tao, L., Huang, G., Song, H., Chen, Y. and Chen, L. (2017). Cancer associated fibroblasts: an essential role in the tumor microenvironment. *Oncol. Lett.* **14**, 2611-2620. doi:10.3892/ol.2017.6497

Theocharidis, G., Drymoussi, Z., Kao, A. P., Barber, A. H., Lee, D. A., Braun, K. M. and Connelly, J. T. (2016). Type VI collagen regulates dermal matrix assembly and fibroblast motility. *J. Investig. Dermatol.* **136**, 74-83. doi:10.1038/JID.2015.352

Tseng, Y., Kole, T. P. and Wirtz, D. (2002). Micromechanical mapping of live cells by multiple-particle-tracking microrheology. *Biophys. J.* **83**, 3162-3176. doi:10.1016/S0006-3495(02)75319-8

Turinetto, V., Vitale, E. and Giachino, C. (2016). Senescence in human mesenchymal stem cells: functional changes and implications in stem cell-based therapy. *Int. J. Mol. Sci.* **17**, E1164. doi:10.3390/ijms17071164

Uccelli, A., Moretta, L. and Pistoia, V. (2008). Mesenchymal stem cells in health and disease. *Nat. Rev. Immunol.* **8**, 726-736. doi:10.1038/nri2395

Vallabhaneni, K. C., Hassler MY, Abraham A, Whitt J, Mo YY, Atfi A, Pochampally R et al. (2016). Mesenchymal stem/stromal cells under stress increase osteosarcoma migration and apoptosis resistance via extracellular vesicle mediated communication. *PLoS ONE* **11**, e0166027. doi:10.1371/journal.pone.0166027

Wagner, W., Bork, S., Horn, P., Krunic, D., Walenda, T., Diehlmann, A., Benes, V., Blake, J., Huber, F.-X., Eckstein, V. et al. (2009). Aging and replicative senescence have related effects on human stem and progenitor cells. *PLoS ONE* **4**, e5846. doi:10.1371/journal.pone.0005846

Wang, N., Tytell, J. D. and Ingber, D. E. (2009). Mechanotransduction at a distance: mechanically coupling the extracellular matrix with the nucleus. *Nat. Rev. Mol. Cell Biol.* **10**, 75-82. doi:10.1038/nrm2594

Wolf, K., Mazo, I., Leung, H., Engelke, K., Von Andrian, U. H., Deryugina, E. I., Strongin, A. Y., Bröcker, E.-B. and Friedl, P. (2003). Compensation mechanism in tumor cell migration: mesenchymal-amoeboid transition after blocking of pericellular proteolysis. *J. Cell Biol.* **160**, 267-277. doi:10.1083/jcb.200209006

Wolf, K., Alexander, S., Schacht, V., Coussens, L. M., von Andrian, U. H., van Rheenen, J., Deryugina, E. and Friedl, P. (2009). Collagen-based cell migration models in vitro and in vivo. *Semin. Cell Dev. Biol.* **20**, 931-941. doi:10.1016/j.semcdb.2009.08.005

Wu, P.-H., Gilkes, D. M. and Wirtz, D. (2018). The Biophysics of 3D Cell Migration. *Ann. Rev. Biophys.* **47**, 549-567. doi:10.1146/annurev-biophys-070816-033854.

Xuan, B., Ghosh, D., Cheney, E. M., Clifton, E. M. and Dawson, M. R. (2018). Dysregulation in actin cytoskeletal organization drives increased stiffness and migratory persistence in polyploidal giant cancer cells. *Sci. Rep.* **8**, 11935. doi:10.1038/s41598-018-29817-5

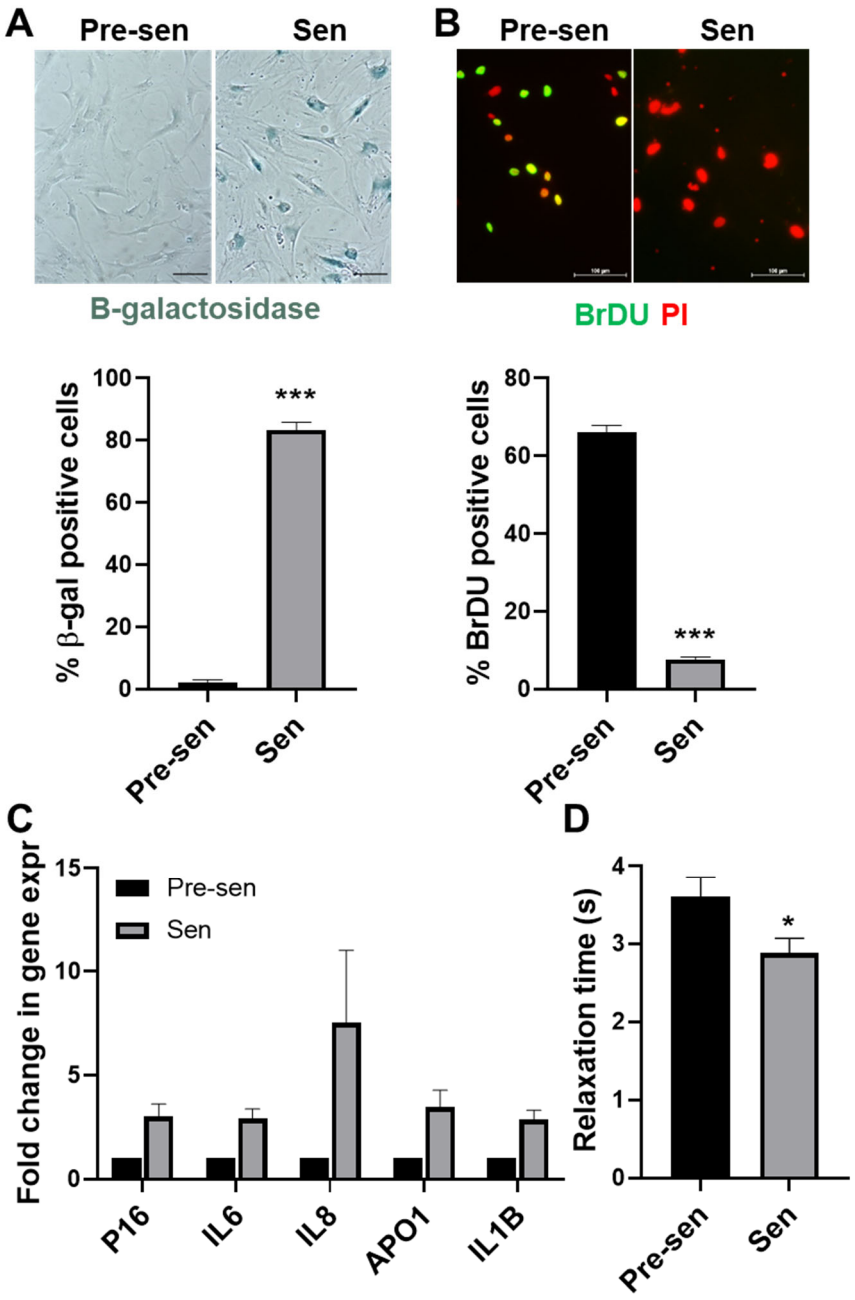

Figure S1. **(A-C) Characterization of radiation induced senescence and development of SASP in MSCs.** Staining and quantification of **(A)** SA-β-galactosidase (blue) and **(B)** BRDU (green: BrDU, red: propidium iodide) incorporation confirmed senescence in irradiated MSCs. **(C)** mRNA expression analysis by qRT-PCR for senescence markers (APO1, P16, IL6, IL8, IL1B); expression of all SASP markers was increased. **(D)** Quantification of average relaxation time (RT) for the nucleus signifying its transition into viscous domain showed significantly lower RT for senescent compared to pre-senescent MSCs. Student's t-tests were used to calculate statistical significance, and p-values less than 0.05 considered significant (*p<0.05, **p<0.01, ***p<0.001).

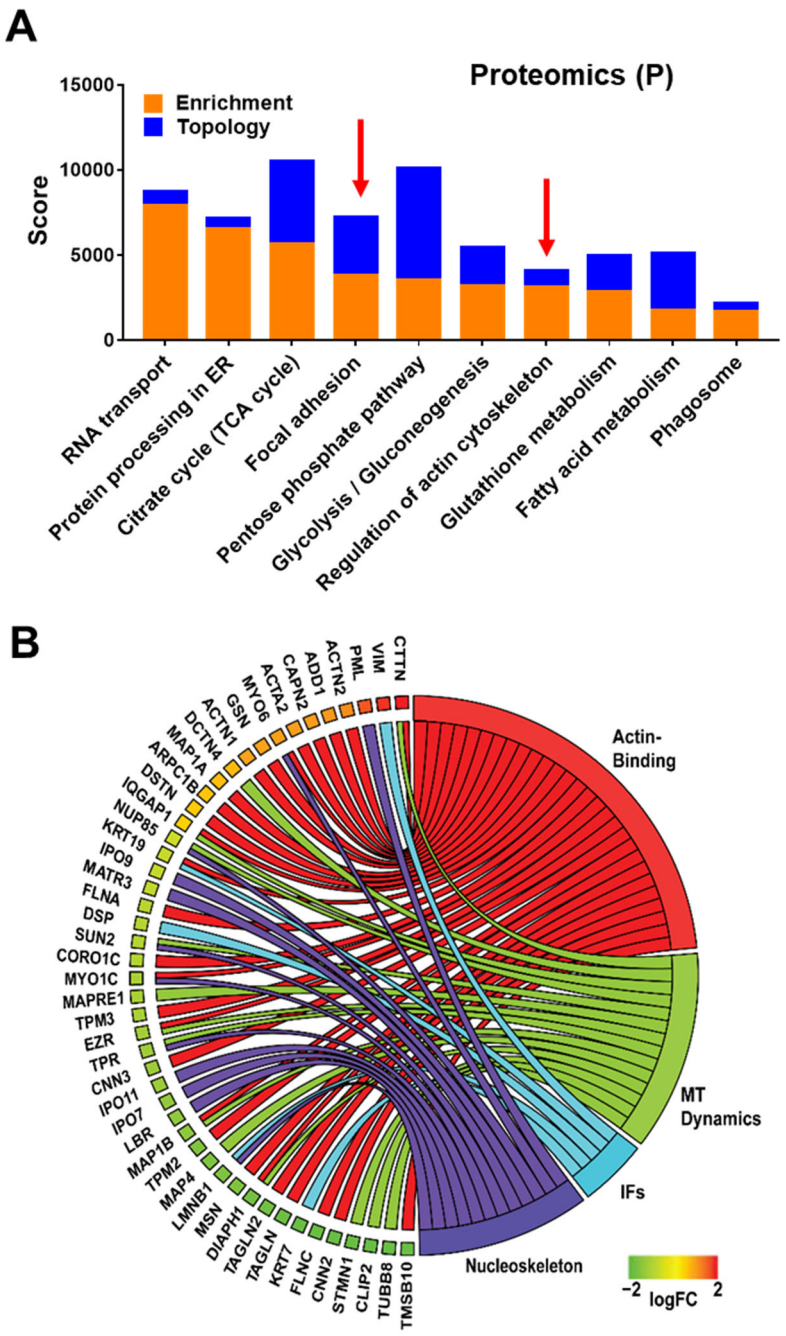

Protein	log2 FC
MCAM	-1.19
ALCAM	-0.83
ZYX	-2.99
ITGB1	0.51
VCL	0.59
ITGBL1	0.79
ITGB5	1.13
ITGA2	1.91

Protein	Log2FC
H2AFV	-1.96
H2AFZ	-2.22
H3F3A	-1.46
HDAC1	-0.92
HIST1H1B	-2.55
HIST1H1C	-3.27
HIST1H1E	-2.03
HIST1H1T	-3.29
HIST1H2BN	-3.00
HIST1H3D	-2.58
HIST1H4A	-1.94

Figure S2. **Pathway analysis of senescence induced changes in protein expression. (A)** Analysis of differentially regulated peptides showed enrichment for pathways including, focal adhesion, and actin cytoskeleton (red arrows). **(B)** GO chord plot of protein expression for senescent versus pre-senescent MSCs are reported for cytoskeleton and nucleoskeleton related proteins (FC-fold change, MT-Microtubule, IF-Intermediate filament). **(C)** Log2 FC in expression for genes related to adhesion and histone modification. **(D)** Western blot was used to analyze expression of LMNA and LMNB1 in senescent MSCs. While LMNA expression was upregulated, LMNB1 was downregulated in senescent MSCs compared to pre-senescent cells.

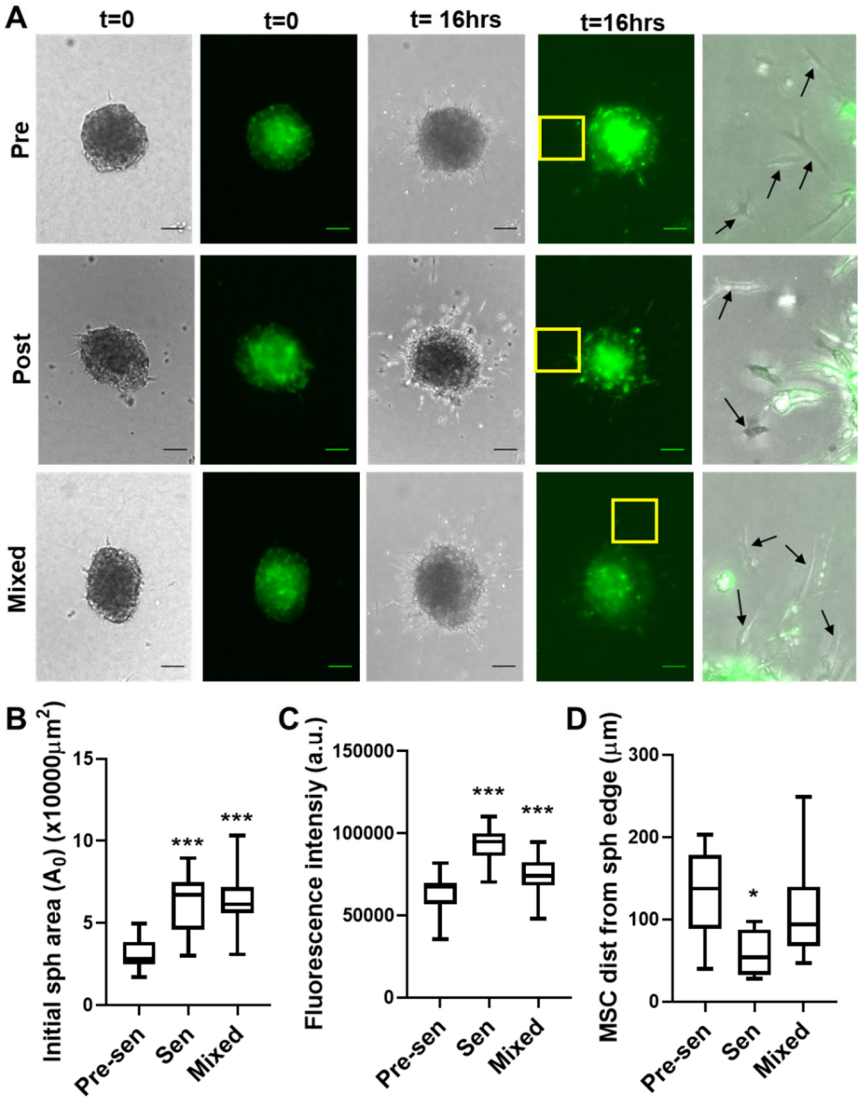

Figure S3. **Comparative role of pre-senescent and senescent MSCs in BCC invasion in 3D collagen gels. (A)** Time-lapsed imaging was used to monitor BCC invasion over 16 hours from spheroids formed with equal numbers of GFP negative MSCs and GFP positive MDA-MB-231 cells and embedded in 1.5 mg/ml collagen gels (Scale bar 100 um). Pre-senescent and senescent MSCs were also combined at 1:1 ratio (mixed). **(B-C)** Initial area (A_0) of the embedded spheroids (**B**) and fluorescence measurement of GFP positive MDA-MB-231 cells (measured with plate reader) (**C**) were quantified to assess the number of BCCs. Presence of senescent cells resulted in spheroids with larger initial area and higher number of BCCs. **(D)** To assess the role of MSCs in invasion, we quantified the invaded distance of MSCs from spheroid boundary. This confirms that pre-senescent MSCs move further from spheroid surface than senescent MSCs. Student's t-tests were used to calculate statistical significance, and p-values less than 0.05 considered significant (*$p < 0.05$, **$p < 0.01$, ***$p < 0.001$).

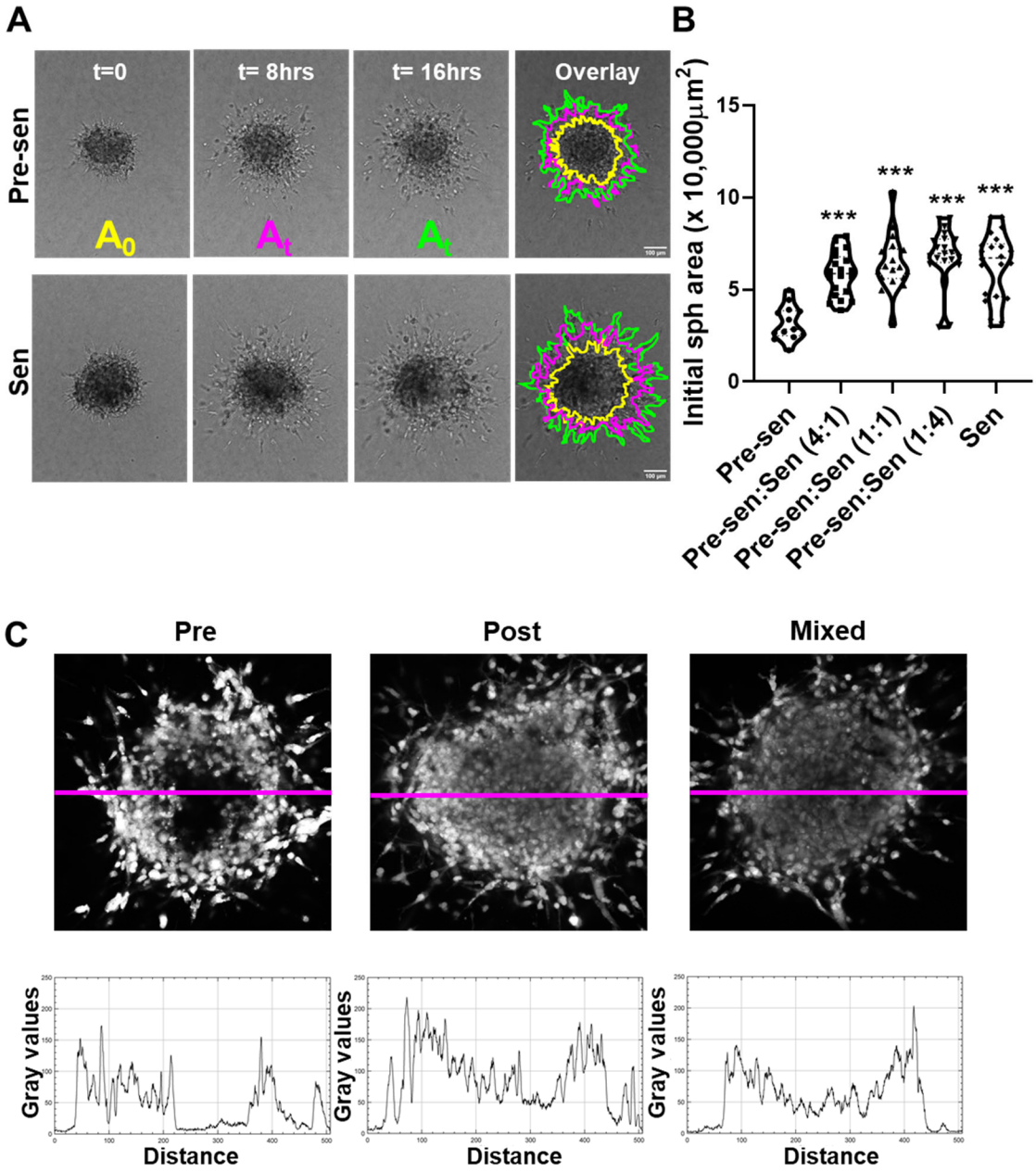

Figure S4. **Role of pre-senescent and senescent MSCs in organization of spheroid and invasion. (A)** Time-lapsed imaging was used to monitor cell migration from spheroids using matrix interface model. Images of spheroid migration over time with regions highlighted in yellow, magenta and green depict the area at times, t= 0, 8 and 16 hours, respectively **(scale bar = 100 μm)**. **(B)** Spheroid area was analyzed for MDA-MB-231 cell spheroids cultured with both individual and mixed population of pre-senescent and senescent MSCs embedded in collagen gels. For the mixed populations, the ratio between MSCs were varied between 4:1 to 1:4. The presence of senescent MSCs increased spheroid size for all ratios compared to spheroids with only pre-senescent MSCs. **(C)** Images from multiphoton confocal microscopy were used to determine cell density distribution in 3D spheroids. The gray intensity representing cell distribution across the central axis (magenta) of the spheroid core was plotted in ImageJ to look at differences in cell density at spheroid core.

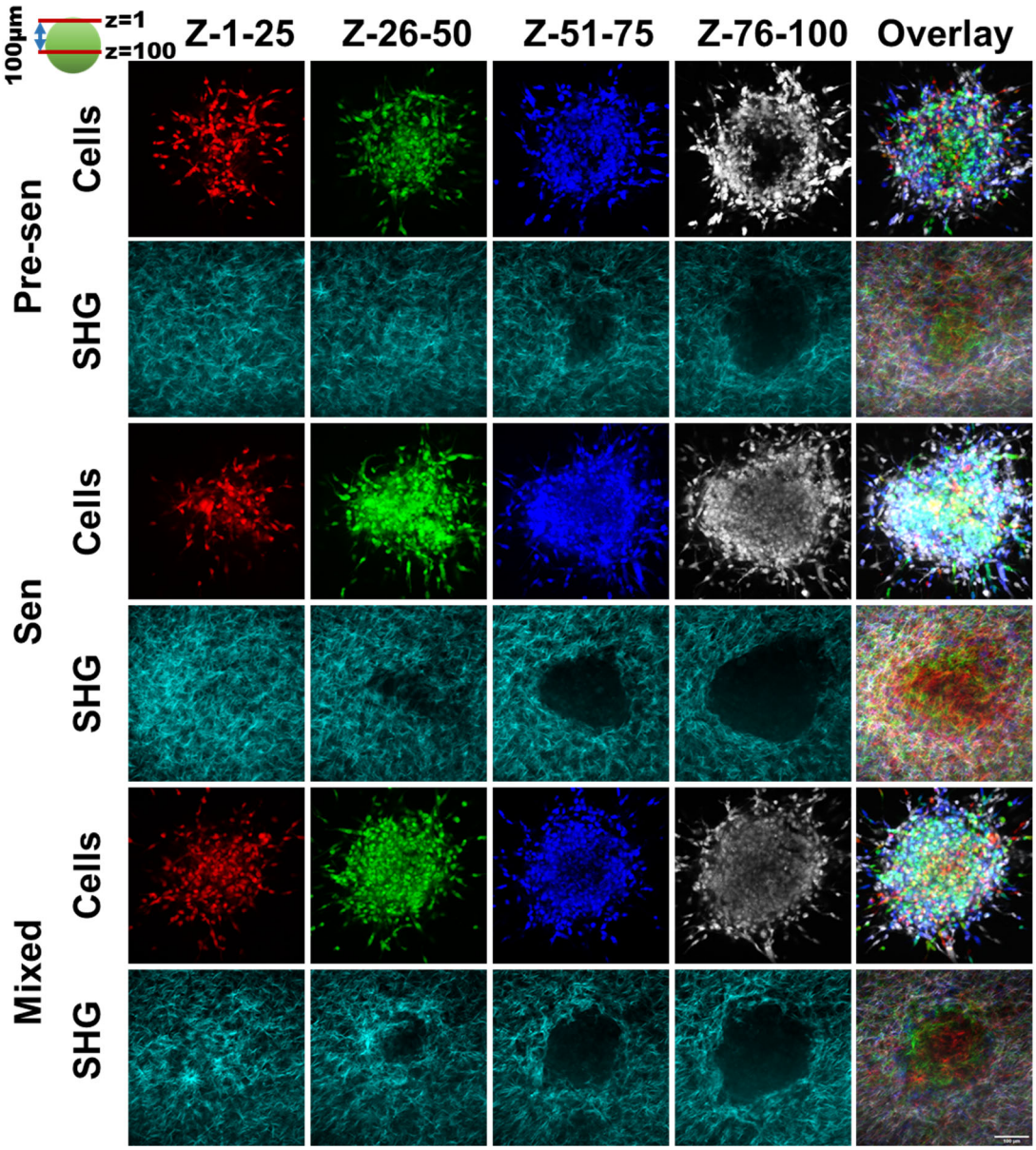

Figure S5. **SHG analysis of collagen structure surrounding spheroids.** Spheroids embedded in collagen gels were imaged by multiphoton microscopy using second harmonic generation to identify collagen (shown in **cyan**) and NucRed to identify cells. Cell z-stacks were color coded (*red: z1-25, green: z26- 50, blue: z51-75, gray: z76-100*) to distinguish different sections of the spheroid **(scale bar=100µm)**. Mosaic images (overlay) of the color-coded sections highlight packing density of spheroids, which is increased for spheroids co-cultured with senescent MSCs.

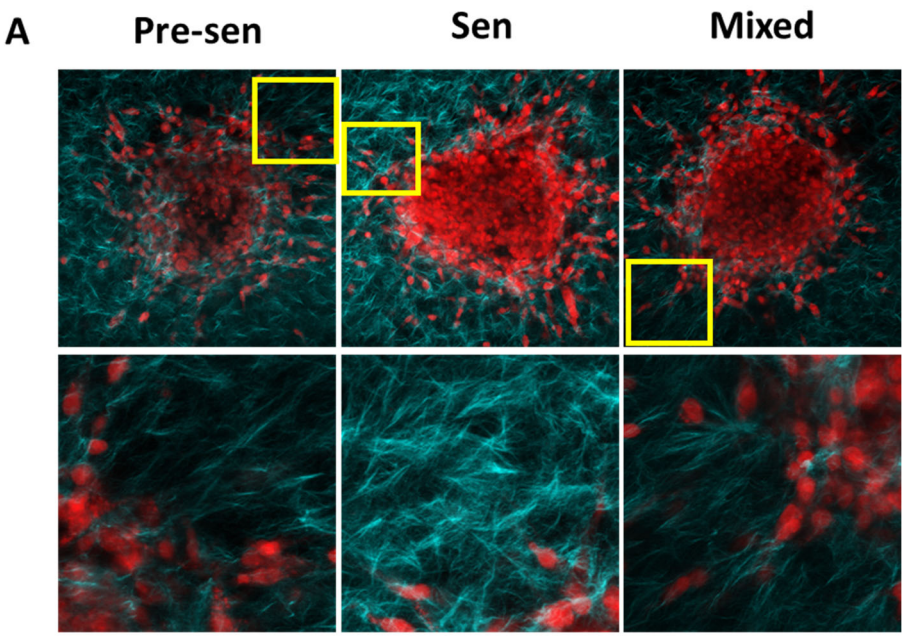

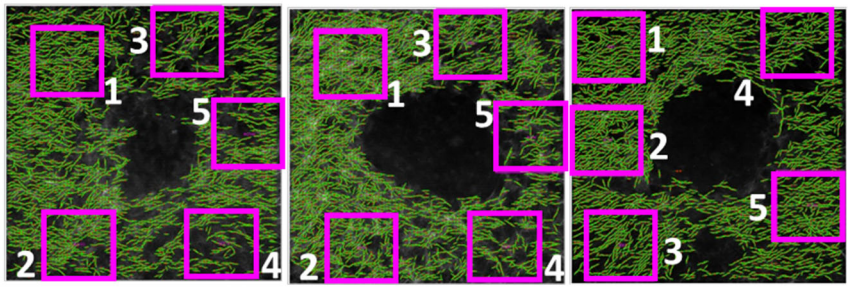

C

ROI label	Align-ment	Box density
ROI1	0.74	84.66
ROI2	0.69	72.79
ROI3	0.61	50.22
ROI4	0.7	46.39
ROI5	0.87	62.11
AVG	0.72	63.23
CV	0.12	0.22
Overall AVG	0.74	63.67

ROI label	Align-ment	Box density
ROI1	0.67	92.56
ROI2	0.48	74.83
ROI3	0.76	65.13
ROI4	0.55	53.42
ROI5	0.73	52.3
AVG	0.64	67.65
CV	0.17	0.22
Overall AVG	0.64	70.2

ROI label	Align-ment	Box density
ROI1	0.77	82.75
ROI2	0.67	85.11
ROI3	0.7	75.61
ROI4	0.67	65.1
ROI5	0.69	75.91
AVG	0.70	76.9
CV	0.05	0.09
Overall AVG	0.69	62.43

Figure S6. **Analysis of local and global structure surrounding spheroids using CT-FIRE.** (**A**) Spheroids embedded in collagen gels were imaged by multiphoton microscopy using second harmonic generation to identify collagen (shown in **cyan**) and NucRed to identify cells (shown in **red**); images include average intensity projections of z-stack and 2D slice for region highlighted by yellow box. (**B-C**) The structure of collagen around the embedded spheroid was analyzed using CurveAlign ROI analysis. For each image, 5 rectangular boxes were selected around the primary spheroid to quantify co-efficient of alignment. Properties of the ROIs along with the overall image are reported here.

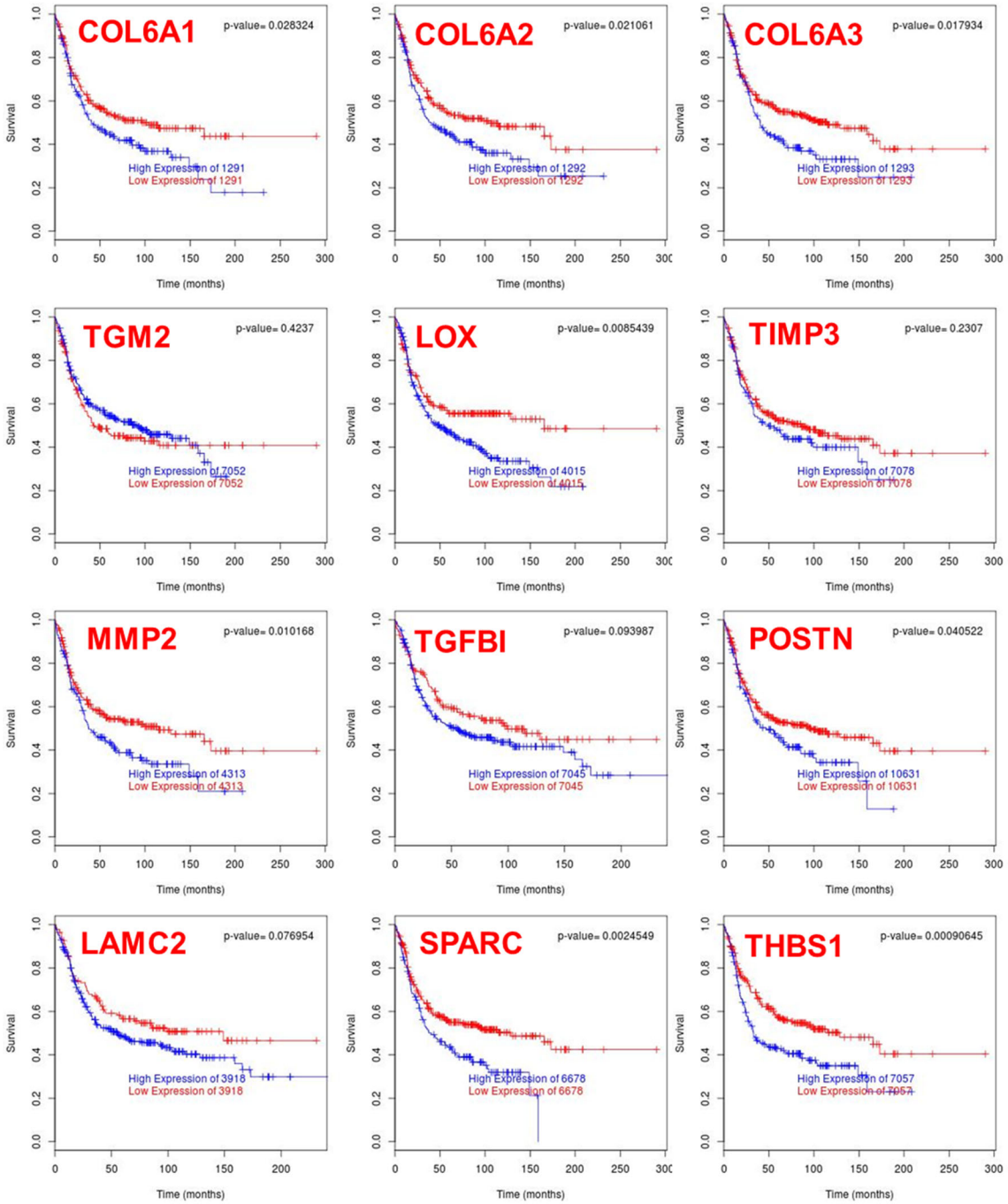

Figure S7. **Survival analysis of senescent associated ECM signature in breast cancer.** ECM signature from senescent MSCs was used to analyze Kaplan-Meier estimates of disease-free survival for breast cancer using free online tool BreastMark at http://glados.ucd.ie/BreastMark/index.html**.** ECM genes upregulated in senescent MSCs including, expression of collagen isoforms (COL6A1, COL6A2, COL6A3), matrix modifying enzymes (LOX, MMP2), and matricellular proteins (POSTN, THBS1, SPARC) are correlated with poor prognosis in basal subtype of breast cancer ($p<0.05$).